



# High-Order Gas-Kinetic Scheme in General Curvilinear Coordinate for iLES of Compressible Wall-Bounded Turbulent Flows

Guiyu Cao<sup>1,2</sup> · Liang Pan<sup>3</sup> · Kun Xu<sup>4</sup> · Shiyi Chen<sup>2</sup>

Received: 8 June 2023 / Revised: 6 April 2024 / Accepted: 8 September 2024 /

Published online: 24 September 2024

© The Author(s), under exclusive licence to Springer Science+Business Media, LLC, part of Springer Nature 2024

## Abstract

In this paper, a high-order gas-kinetic scheme in general curvilinear coordinate (HGKS-cur) is developed for the numerical simulation of compressible turbulence. Based on the coordinate transformation, the Bhatnagar-Gross-Krook (BGK) equation is transformed from physical space to computational space. To deal with the general mesh given by discretized points, the geometrical metrics need to be constructed by the dimension-by-dimension Lagrangian interpolation. The multidimensional weighted essentially non-oscillatory (WENO) reconstruction is adopted in the computational domain for spatial accuracy, where the reconstructed variables are the cell averaged Jacobian and the Jacobian-weighted conservative variables. The two-stage fourth-order method, which was developed for spatial-temporal coupled flow solvers, is used for temporal discretization. The numerical examples for inviscid and laminar flows validate the accuracy and geometrical conservation law of HGKS-cur. As a direct application, HGKS-cur is implemented for the implicit large eddy simulation (iLES) in compressible wall-bounded turbulent flows, including the compressible turbulent channel flow and compressible turbulent flow over periodic hills. The iLES results with HGKS-cur are in good agreement with the refereed spectral methods and high-order finite volume methods. The performance of HGKS-cur definitely demonstrates its capability as a powerful tool for

---

✉ Liang Pan  
panliang@bnu.edu.cn

✉ Shiyi Chen  
chensy@sustc.edu.cn

Guiyu Cao  
guiyu.cao@eng.ox.ac.uk

Kun Xu  
makxu@ust.hk

<sup>1</sup> Department of Engineering Science, University of Oxford, Oxford, UK

<sup>2</sup> Academy for Advanced Interdisciplinary Studies, Southern University of Science and Technology, Shenzhen, China

<sup>3</sup> Laboratory of Mathematics and Complex Systems, School of Mathematical Sciences, Beijing Normal University, Beijing, China

<sup>4</sup> Department of Mathematics, Hong Kong University of Science and Technology, Clear Water Bay, Kowloon, Hong Kong

the iLES of compressible wall-bounded turbulent flows and massively separated flows with curved boundary.

**Keywords** High-order gas-kinetic scheme · General curvilinear coordinate · Implicit large eddy simulation · Wall-bounded turbulent flows · Compressible turbulence

## 1 Introduction

The understanding and prediction of multi-scale turbulent flows is one of the most difficult problems in both mathematics and physical sciences. With the development of numerical methods and super computers, great successes have been achieved by the numerical simulation of unsteady turbulent flows. Conceptually, the direct numerical simulation (DNS) [1, 2] is supposed to resolve turbulent structures above the Kolmogorov dissipation scale by using resolved grid size and time step, which solves the Navier–Stokes equations directly and eliminates modeling entirely. But the extremely expensive computational costs prohibit its application in high-Reynolds number turbulent flows. In order to study turbulent flows on the unresolved grids, the large eddy simulation (LES) [3, 4] have been developed. LES solves the filtered Navier–Stokes equations with resolvable turbulent structures above the inertial scale. For unsteady separated turbulent flows, LES has gradually become an indispensable tool to obtain high-resolution turbulent flow fields. The high-order numerical schemes play a key role in the numerical simulation of turbulence. In the past few decades, the spectral method [1] and the pseudo-spectral method [5] have been well established as a powerful DNS tool for the incompressible turbulent flows [6]. For the simulation of near incompressible turbulence, the lattice Boltzmann method [7, 8] is widely used. Unfortunately, for the simulation of compressible turbulence with discontinuity, the shocklets may appear in the flow fields and all of them suffer from numerical instability. With the properties of high-order accuracy in smooth region and no oscillation near shocks, the high-order finite difference method [9–11] have been widely developed and utilized for compressible turbulence simulation with discontinuities [12, 13].

Due to the significance of engineering applications and the study on fundamental physical mechanism of compressible boundary layer, the compressible wall-bounded turbulent flows have been extensively simulated using the high-order schemes. The representative research are briefly presented as follows: the compressible turbulent channel flow from the supersonic to hypersonic regime [14–16], the supersonic and hypersonic flat plate turbulence [17–19], the compressible separated turbulent flow over periodic hills [20–23], and the compression ramp [24–26] with shock-boundary interactions. The high-order finite difference methods are dominated in the simulation of compressible wall-bounded turbulence, except the temporal supersonic turbulent channel flow can be simulated by spectral method [14]. Even for the hypersonic flat plate turbulence with free-stream Mach number  $Ma = 8.0$ , the maximum turbulent Mach number  $M_t$  is less than 0.5 [18], which means no strong shock-lets in such cases. This is the key reason why the high-order finite difference methods are the main workhorse in compressible wall-bounded turbulence simulations. However, due to the numerical instability when encountering strong shocklets, the highest turbulent Mach number for high-order finite difference scheme is still limited, and the critical threshold of simulating supersonic flow remains, i.e., turbulent Mach number  $M_t \leq 1.2$  for DNS of supersonic isotropic turbulence [13]. Besides, to simulate the hypersonic flows robustly, the complicated artificial viscosity and artificial heat conductivity are usually constructed in high-order finite

difference method [19]. Because of the excellent conservative properties and favorable ability in capturing strong discontinuities, high-order finite volume scheme may pave a new way for high-resolution simulation of turbulent flows in all flow regimes from subsonic to supersonic ones [27–29].

In the past decades, the finite-volume gas-kinetic scheme (GKS) based on the Bhatnagar-Gross-Krook (BGK) model [32, 33] have been developed systematically for computations from low speed flows to supersonic ones [34, 35]. The GKS presents a gas evolution process from kinetic scale to hydrodynamic scale, where both inviscid and viscous fluxes are recovered from a time-dependent and multi-dimensional gas distribution function at a cell interface. Based on the time-dependent flux function, a reliable two-stage framework was provided for developing the GKS into fourth-order and even higher-order accuracy [36–39]. More importantly, the high-order GKS (HGKS) is as robust as the second-order scheme and works perfectly from the subsonic to the hypersonic viscous flows. With the advantage of the finite-volume GKS, it has been developed as a powerful tool to simulate turbulent flows. For high-Reynolds number engineering turbulence, the GKS coupled with traditional eddy viscosity turbulence model has been developed and implemented in turbulence simulations [40–42]. For low-Reynolds number turbulent flows, the HGKS has been directly used as a DNS tool [27, 28]. Recently, a parallel code of HGKS is developed for the large-scale DNS, where the domain decomposition and message passing interface (MPI) is used for parallel implementation [28]. The computational cost is comparable with the high-order finite difference method. For the nearly incompressible turbulent flows, the performance of HGKS is also comparable with the finite difference method. More importantly, HGKS shows special advantages for the supersonic turbulence due to the accuracy and robustness, i.e., the supersonic isotropic turbulence with turbulent Mach number  $M_t = 2.0$  has been simulated successfully [29]. For the compressible Taylor-Green vortex problem, the quantitative comparisons are conducted between implicit large eddy simulation (iLES) and explicit eddy-viscosity large eddy simulation (eLES) with HGKS [30]. Compared with the key statistical quantities of direct numerical simulation, iLES outweighs eLES on the exactly same unresolved grids.

In previous study [43], the high-order gas-kinetic scheme has been developed in the curvilinear coordinate for laminar flows, in which the coordinate transformations are given analytically. However, for more turbulent cases, the grid points are given by the discretized points and there is no analytical transformation. In this paper, the HGKS in general curvilinear coordinate (HGKS-cur) will be presented within the two-stage fourth-order framework for the first time. The curvilinear meshes can be given analytically or in the form of discretized grid points without analytical transformation. With the discretized grid points, the geometric metrics can be constructed by the dimension-by-dimension Lagrangian interpolation. The numerical results validate that the geometrical conservation law can be well preserved. The weighted essentially non-oscillatory (WENO) reconstruction [44, 45] is adopted in the computational domain for spatial accuracy, where the reconstructed variables are the cell averaged Jacobian and the Jacobian-weighted conservative variables. The two-stage fourth-order method [36], which was developed for spatial-temporal coupled flow solvers, is used for temporal discretization. The direct numerical simulation is very computationally intensive, so the HGKS-cur with LES is considered for turbulence simulation in the current work. Due to the lower computational cost and high-order accuracy, the iLES has been widely used in turbulence simulation [46–50]. For iLES, the built-in numerical dissipation acts as the subgrid-scale (SGS) dissipation, thus no explicit SGS model need to be utilized. In the previous work [30], the iLES outperforms the eLES on the exact same unresolved grids with HGKS. The iLES approach can overcome the problem of over-dissipation that occurs in eLES models. In view of the superior performance of iLES with HGKS, we investigate the

high-accuracy strength of the HGKS-cur in the iLES of turbulent flows with curved boundary. The compressible wall-bounded turbulent flows, including the compressible turbulent channel flow and compressible turbulent flow over periodic hills, are simulated. The performance of HGKS-cur shows its great capability for the iLES of compressible wall-bounded turbulent flows with curved boundary.

This paper is organized as follows. The high-order gas-kinetic scheme in general curvilinear coordinate will be provided in Sect. 2. Numerical examples and discussions are included in Sect. 3. The last section is the conclusion.

## 2 High-Order Gas-Kinetic Scheme in General Curvilinear Coordinate

### 2.1 BGK Equation and Coordinate Transformation

The three-dimensional BGK equation [32] can be written as

$$f_t + u f_x + v f_y + w f_z = \frac{g - f}{\tau}, \quad (1)$$

where  $\mathbf{u} = (u, v, w)^T$  is the particle velocity,  $f$  is the three-dimensional gas distribution function,  $g$  is the three-dimensional Maxwellian distribution and  $\tau$  is the collision time. The collision term satisfies the compatibility condition

$$\int \frac{g - f}{\tau} \psi d\Xi = 0, \quad (2)$$

where  $\psi = (1, u, v, w, \frac{1}{2}(u^2 + v^2 + w^2 + \zeta^2))^T$ , the internal variables  $\zeta^2 = \zeta_1^2 + \dots + \zeta_N^2$ ,  $d\Xi = du dv dw d\zeta^1 \dots d\zeta^N$ ,  $\gamma$  is the specific heat ratio and  $N = (5 - 3\gamma)/(\gamma - 1)$  is the internal degrees of freedom for three-dimensional flows. According to the Chapman-Enskog expansion for BGK equation, the Euler and Navier–Stokes equations can be derived [33, 34].

To construct the numerical scheme in general curvilinear coordinate, a coordinate transformation from physical domain  $(x, y, z)$  to computational domain  $(\xi, \eta, \zeta)$  is given by

$$\left( \frac{\partial(x, y, z)}{\partial(\xi, \eta, \zeta)} \right) = \begin{pmatrix} x_\xi & x_\eta & x_\zeta \\ y_\xi & y_\eta & y_\zeta \\ z_\xi & z_\eta & z_\zeta \end{pmatrix}. \quad (3)$$

With above transformation, the BGK equation Eq.(1) can be transformed as

$$\begin{aligned} \frac{\partial}{\partial t} (\mathcal{J} f) + \frac{\partial}{\partial \xi} ([u \widehat{\xi}_x + v \widehat{\xi}_y + w \widehat{\xi}_z] f) + \frac{\partial}{\partial \eta} ([u \widehat{\eta}_x + v \widehat{\eta}_y + w \widehat{\eta}_z] f) \\ + \frac{\partial}{\partial \zeta} ([u \widehat{\zeta}_x + v \widehat{\zeta}_y + w \widehat{\zeta}_z] f) = \frac{g - f}{\tau} \mathcal{J}, \end{aligned} \quad (4)$$

where  $\mathcal{J}$  is the Jacobian of transformation and the metrics above are given as follows

$$\begin{pmatrix} \widehat{\xi}_x & \widehat{\xi}_y & \widehat{\xi}_z \\ \widehat{\eta}_x & \widehat{\eta}_y & \widehat{\eta}_z \\ \widehat{\zeta}_x & \widehat{\zeta}_y & \widehat{\zeta}_z \end{pmatrix} = \begin{pmatrix} y_\eta z_\zeta - z_\eta y_\zeta & z_\eta x_\zeta - x_\eta z_\zeta & x_\eta y_\zeta - y_\eta x_\zeta \\ y_\zeta z_\xi - z_\zeta y_\xi & z_\zeta x_\xi - x_\zeta z_\xi & x_\zeta y_\xi - y_\zeta x_\xi \\ y_\xi z_\eta - z_\xi y_\eta & z_\xi x_\eta - x_\xi z_\eta & x_\xi y_\eta - y_\xi x_\eta \end{pmatrix}. \quad (5)$$

Taking moments and integrating Eq.(4) over the control volume  $V_{ijk}$ , the semi-discretized finite volume scheme reads

$$\frac{d\widehat{Q}_{ijk}}{dt} = \mathcal{L}(\widehat{Q}_{ijk}) = -\frac{1}{|V_{ijk}|} \left[ \int_{\eta_j-\Delta\eta/2}^{\eta_j+\Delta\eta/2} \int_{\zeta_k-\Delta\zeta/2}^{\zeta_k+\Delta\zeta/2} (\widehat{\mathbb{F}}_{i+1/2,j,k} - \widehat{\mathbb{F}}_{i-1/2,j,k}) d\eta d\zeta \right. \\ \left. + \int_{\xi_i-\Delta\xi/2}^{\xi_i+\Delta\xi/2} \int_{\zeta_k-\Delta\zeta/2}^{\zeta_k+\Delta\zeta/2} (\widehat{\mathbb{G}}_{i,j+1/2,k} - \widehat{\mathbb{G}}_{i,j-1/2,k}) d\xi d\zeta \right. \\ \left. + \int_{\xi_i-\Delta\xi/2}^{\xi_i+\Delta\xi/2} \int_{\eta_j-\Delta\eta/2}^{\eta_j+\Delta\eta/2} (\widehat{\mathbb{H}}_{i,j,k+1/2} - \widehat{\mathbb{H}}_{i,j,k-1/2}) d\xi d\eta \right], \quad (6)$$

where the mesh is uniformly distributed in the computational domain for simplicity,  $|V_{ijk}| = \Delta\xi\Delta\eta\Delta\zeta$  and the Jacobian weighted conservative variable in Eq.(6) is defined as

$$\widehat{Q}_{ijk} = \frac{1}{|V_{ijk}|} \int_{V_{ijk}} \int \psi \mathcal{J} f d\Xi d\xi d\eta d\zeta.$$

## 2.2 Gas-Kinetic Solver

For the finite volume method, the key procedure is updating the conservative flow variables inside each control volume through the numerical fluxes. The flux in  $\xi$ -direction is given as an example and Gaussian quadrature is used as

$$\widehat{\mathbb{F}}_{i+1/2,j,k} \\ = \int_{\eta_j-\Delta\eta/2}^{\eta_j+\Delta\eta/2} \int_{\zeta_k-\Delta\zeta/2}^{\zeta_k+\Delta\zeta/2} \widehat{\mathbb{F}}_{i+1/2,j,k} d\eta d\zeta = \Delta\eta\Delta\zeta \sum_{m,n=1}^2 \omega_{mn} S_{mn} F(\xi_{i+1/2,j_m,k_n}, t). \quad (7)$$

For each Gaussian quadrature point of cell interface, the geometrical metric  $S = \sqrt{\widehat{\xi}_x^2 + \widehat{\xi}_y^2 + \widehat{\xi}_z^2}$ , and the local particle velocity  $\tilde{\mathbf{u}}$  is given by

$$\tilde{\mathbf{u}} = (\tilde{u}, \tilde{v}, \tilde{w}) = (u, v, w) \cdot (\mathbf{n}_x, \mathbf{n}_y, \mathbf{n}_z),$$

where  $\mathbf{n}_x = (\widehat{\xi}_x, \widehat{\xi}_y, \widehat{\xi}_z) / \sqrt{\widehat{\xi}_x^2 + \widehat{\xi}_y^2 + \widehat{\xi}_z^2}$  is the normal direction and  $\mathbf{n}_y, \mathbf{n}_z$  are two orthogonal tangential directions at each Gaussian quadrature point. For gas-kinetic solver, the time dependent numerical flux can be given by

$$F(\xi_{i+1/2,j_m,k_n}, t) = \int \tilde{u} \psi f(\mathbf{x}_{i+1/2,j_m,k_n}, t, \tilde{\mathbf{u}}, \varsigma) d\widetilde{\Xi},$$

where  $d\widetilde{\Xi} = d\tilde{u} d\tilde{v} d\tilde{w} d\tilde{\zeta}^1 \cdots d\tilde{\zeta}^N$  and the gas distribution function  $f(\mathbf{x}_{i+1/2,j_m,k_n}, t, \mathbf{u}, \varsigma)$  can be given by the integral solution of BGK equation as Eq.(1)

$$f(\mathbf{x}_{i+1/2,j_m,k_n}, t, \mathbf{u}, \varsigma) = \frac{1}{\tau} \int_0^t g(\mathbf{x}', t', \mathbf{u}, \varsigma) e^{-(t-t')/\tau} dt' + e^{-t/\tau} f_0(-\mathbf{u}t, \varsigma), \quad (8)$$

where  $\mathbf{x}' = \mathbf{x}_{i+1/2,j_m,k_n} - \mathbf{u}(t-t')$  is the trajectory of particles,  $\tilde{\mathbf{u}}$  is denoted as  $\mathbf{u}$  for simplicity,  $f_0$  is the initial gas distribution function and  $g$  is the corresponding equilibrium state. For a multi-dimensional second-order gas-kinetic solver [35],  $g$  and  $f_0$  can be constructed as

$$g = g_0(1 + \bar{a}x + \bar{b}y + \bar{c}z + \bar{A}t),$$

and

$$f_0 = \begin{cases} g_l[1 + (a_l x + b_l y + c_l z) - \tau(a_l u + b_l v + c_l w + A_l)], & x \leq 0, \\ g_r[1 + (a_r x + b_r y + c_r z) - \tau(a_r u + b_r v + c_r w + A_r)], & x > 0, \end{cases}$$

where  $g_l$  and  $g_r$  are the initial equilibrium gas distribution functions on both sides of a cell interface, and  $g_0$  is the initial equilibrium state located at cell interface, which can be determined through the compatibility condition as Eq.(2). Substituting  $g$  and  $f_0$  into Eq.(8), the second-order gas distribution function at cell interface can be constructed as

$$\begin{aligned} f(\mathbf{x}_{i+1/2, j_m, k_n}, t, \mathbf{u}, \varsigma) = & (1 - e^{-t/\tau})g_0 + ((t + \tau)e^{-t/\tau} - \tau)(\bar{a}u + \bar{b}v + \bar{c}w)g_0 \\ & + (t - \tau + \tau e^{-t/\tau})\bar{A}g_0 \\ & + e^{-t/\tau}g_l[1 - (\tau + t)(a_l u + b_l v + c_l w) - \tau A^l]H(u) \\ & + e^{-t/\tau}g_r[1 - (\tau + t)(a_r u + b_r v + c_r w) - \tau A^r](1 - H(u)). \end{aligned} \quad (9)$$

Eq.(9) presents a gas evolution process from kinetic scale to hydrodynamic scale, where both inviscid and viscous fluxes are recovered from a time-dependent and multi-dimensional gas distribution function at a cell interface.

In a well-resolved region with continuous flow distributions across a cell interface, i.e.  $g_l = g_r$ ,  $a_l = a_r = \bar{a}$ ,  $b_l = b_r = \bar{b}$ ,  $c_l = c_r = \bar{c}$ ,  $A_l = A_r = \bar{A}$ . For the viscous flows, in a well-resolved region, the second-order gas-kinetic flux Eq.(9) is simplified as

$$f(\mathbf{x}_{i+1/2, j_m, k_n}, t, \mathbf{u}, \varsigma) = g(1 - \tau(\bar{a}u + \bar{b}v + \bar{c}w + A) + At). \quad (10)$$

Compared with Eq.(9), Eq.(10) is much more efficient and much lower dissipative. In this paper, we mainly focus on the smooth solutions, and Eq.(10) is used for the computation of numerical fluxes. Meanwhile, for the flow with discontinuities [27, 29], Eq.(9) has to be used to provide the multiple gas evolution process.

More details of the second-order gas-kinetic solver can be found in refereed paper [34, 35]. To achieve high-order accuracy in space and time, the high-order spatial reconstruction and the multi-stage time discretization will be provided in the following subsections.

## 2.3 Spatial Reconstruction

High-order gas-kinetic scheme has been developed in the curvilinear coordinate [43], where the coordinate transformations are given analytically. For these cases, the terms in Eq.(3) at quadrature points can be calculated by taking derivatives of the transformation directly, and the geometrical conservation law can be preserved automatically. In general curvilinear coordinate, the grid points are given by the discretized points and there is no analytical transformation. In addition, the reconstruction of geometrical metrics is also needed to achieve the spatial accuracy and geometrical conservation law.

As preparation, the derivative terms can be given by the Lagrangian interpolation at each grid point

$$\begin{aligned} (\mathbf{x}_\xi)_{ijk} &= \frac{1}{12\Delta\xi} \left( 8(\mathbf{x}_{i+1,j,k} - \mathbf{x}_{i-1,j,k}) - (\mathbf{x}_{i+2,j,k} - \mathbf{x}_{i-2,j,k}) \right), \\ (\mathbf{x}_\eta)_{ijk} &= \frac{1}{12\Delta\eta} \left( 8(\mathbf{x}_{i,j+1,k} - \mathbf{x}_{i,j-1,k}) - (\mathbf{x}_{i,j+2,k} - \mathbf{x}_{i,j-2,k}) \right), \\ (\mathbf{x}_\zeta)_{ijk} &= \frac{1}{12\Delta\zeta} \left( 8(\mathbf{x}_{i,j,k+1} - \mathbf{x}_{i,j,k-1}) - (\mathbf{x}_{i,j,k+2} - \mathbf{x}_{i,j,k-2}) \right), \end{aligned} \quad (11)$$

where  $\mathbf{x}_{ijk} = (x, y, z)_{ijk}$  is the coordinate of each grid point. To preserve the geometric conservation law (GCL) [11, 51], each term in Eq.(5) should be evaluated by the symmetric conservative forms, and  $(\widehat{\xi}_x, \widehat{\xi}_y, \widehat{\xi}_z)$  is given as an example

$$\begin{aligned}\widehat{\xi}_x &= \frac{1}{2}((zy_\eta)_\zeta - (yz_\eta)_\zeta + (zy_\zeta)_\eta - (yz_\zeta)_\eta), \\ \widehat{\xi}_y &= \frac{1}{2}((xz_\eta)_\zeta - (zx_\eta)_\zeta + (zx_\zeta)_\eta - (zx_\zeta)_\eta), \\ \widehat{\xi}_z &= \frac{1}{2}((yx_\eta)_\zeta - (xy_\eta)_\zeta + (yx_\zeta)_\eta - (xy_\zeta)_\eta),\end{aligned}\quad (12)$$

where the terms  $zy_\eta, yz_\eta, zy_\zeta, yz_\zeta, \dots$  at the grid point can be prepared by  $\mathbf{x}_{ijk}$  and Eq.(11) for  $(\mathbf{x}_\xi)_{ijk}, (\mathbf{x}_\eta)_{ijk}, (\mathbf{x}_\zeta)_{ijk}$ . The next step is the dimension-by-dimension Lagrangian interpolation from the grid points to the quadrature points, and two-point Gaussian quadrature is used for spatial accuracy. The interpolated variables and their spatial derivatives can be given by

$$\begin{aligned}\boldsymbol{\alpha}_1 &= \frac{1}{216}((-9 - \sqrt{3})\boldsymbol{\alpha}_{i-1} + (117 + 39\sqrt{3})\boldsymbol{\alpha}_i + (117 - 39\sqrt{3})\boldsymbol{\alpha}_{i+1} + (\sqrt{3} - 9)\boldsymbol{\alpha}_{i+2}), \\ \boldsymbol{\alpha}_2 &= \frac{1}{216}((\sqrt{3} - 9)\boldsymbol{\alpha}_{i-1} + (117 - 39\sqrt{3})\boldsymbol{\alpha}_i + (117 + 39\sqrt{3})\boldsymbol{\alpha}_{i+1} + (-9 - \sqrt{3})\boldsymbol{\alpha}_{i+2}),\end{aligned}$$

and

$$\begin{aligned}(\boldsymbol{\alpha}_\eta)_1 &= \frac{1}{12\Delta\eta}(-\sqrt{3}\boldsymbol{\alpha}_{i-1} - (12 - \sqrt{3})\boldsymbol{\alpha}_i + (12 + \sqrt{3})\boldsymbol{\alpha}_{i+1} - \sqrt{3}\boldsymbol{\alpha}_{i+2}), \\ (\boldsymbol{\alpha}_\eta)_2 &= \frac{1}{12\Delta\eta}(\sqrt{3}\boldsymbol{\alpha}_{i-1} - (12 + \sqrt{3})\boldsymbol{\alpha}_i + (12 - \sqrt{3})\boldsymbol{\alpha}_{i+1} + \sqrt{3}\boldsymbol{\alpha}_{i+2}),\end{aligned}$$

where  $\boldsymbol{\alpha}$  represents the variables for interpolation, i.e.  $zy_\eta, yz_\eta, zy_\zeta, yz_\zeta, \dots$ . Thus, the variables in Eq.(12) can be given at Gaussian quadrature point.

In the computation, the cell averaged Jacobian and Jacobian weighted conservative variables are needed for spatial reconstruction, and both of them are given according to the following quadrature rule

$$\begin{aligned}\widehat{\mathcal{J}}_{ijk} &= \int_{V_{ijk}} \mathcal{J} d\xi d\eta d\zeta = \sum_{l,m,n} \mathcal{J}_{l,m,n} \Delta\xi \Delta\eta \Delta\zeta, \\ \widehat{\mathcal{Q}}_{ijk} &= \int_{V_{ijk}} \mathcal{J} Q d\xi d\eta d\zeta = \sum_{l,m,n} (\mathcal{J} Q)_{l,m,n} \Delta\xi \Delta\eta \Delta\zeta,\end{aligned}$$

where the subscripts  $(l, m, n)$  represent the index of three-dimensional Gaussian quadrature points for cell  $V_{ijk}$ . For the high-order spatial accuracy, the fifth-order WENO method [44, 45] is adopted, and the dimension-by-dimension reconstruction is applied for the three-dimensional computation. With the WENO reconstruction of  $\widehat{\mathcal{J}}$  and  $\widehat{\mathcal{Q}}$ , the point value of  $(\mathcal{J} Q)$ ,  $\mathcal{J}$  can be reconstructed at each Gaussian quadrature points of cell interface, and the point value  $Q$  can be calculated by

$$Q = \frac{(\mathcal{J} Q)}{\mathcal{J}}.$$

For the numerical scheme with Riemann solvers, the numerical fluxes can be fully given by the reconstructed conservative variables at both side of cell interface. However, for the gas-kinetic solver, the spatial derivatives of the conservative variables at Gaussian quadrature points are

also needed for the time dependent evolution. The spatial reconstruction is performed in the computational space, and  $Q_\xi$ ,  $Q_\eta$ ,  $Q_\zeta$  can be obtained by the chain rule

$$\begin{aligned}\frac{(\mathcal{J}Q)_\xi - Q\mathcal{J}_\xi}{\mathcal{J}} &= Q_\xi = Q_x x_\xi + Q_y y_\xi + Q_z z_\xi, \\ \frac{(\mathcal{J}Q)_\eta - Q\mathcal{J}_\eta}{\mathcal{J}} &= Q_\eta = Q_x x_\eta + Q_y y_\eta + Q_z z_\eta, \\ \frac{(\mathcal{J}Q)_\zeta - Q\mathcal{J}_\zeta}{\mathcal{J}} &= Q_\zeta = Q_x x_\zeta + Q_y y_\zeta + Q_z z_\zeta.\end{aligned}$$

The directional derivatives can be normalized as follows

$$\begin{aligned}Q_{\xi'} &= Q_\xi / |\mathbf{x}_\xi|, \quad \boldsymbol{\tau}_1 = (x_\xi, y_\xi, z_\xi) / |\mathbf{x}_\xi|, \\ Q_{\eta'} &= Q_\eta / |\mathbf{x}_\eta|, \quad \boldsymbol{\tau}_2 = (x_\eta, y_\eta, z_\eta) / |\mathbf{x}_\eta|, \\ Q_{\zeta'} &= Q_\zeta / |\mathbf{x}_\zeta|, \quad \boldsymbol{\tau}_3 = (x_\zeta, y_\zeta, z_\zeta) / |\mathbf{x}_\zeta|,\end{aligned}$$

where  $\boldsymbol{\tau}_1, \boldsymbol{\tau}_2, \boldsymbol{\tau}_3$  can be obtained from the coordinate transformation. For the general curvilinear coordinate, they are not orthogonal and  $\boldsymbol{\tau}_i$  can be presented as

$$\boldsymbol{\tau}_i = (\boldsymbol{\tau}_i, \mathbf{n}_x)\mathbf{n}_x + (\boldsymbol{\tau}_i, \mathbf{n}_y)\mathbf{n}_y + (\boldsymbol{\tau}_i, \mathbf{n}_z)\mathbf{n}_z.$$

The spatial derivatives in the local orthogonal coordinate are fully determined by the following relation

$$\begin{aligned}Q_{\xi'} &= (\boldsymbol{\tau}_1, \mathbf{n}_x) \frac{\partial Q}{\partial \mathbf{n}_x} + (\boldsymbol{\tau}_1, \mathbf{n}_y) \frac{\partial Q}{\partial \mathbf{n}_y} + (\boldsymbol{\tau}_1, \mathbf{n}_z) \frac{\partial Q}{\partial \mathbf{n}_z}, \\ Q_{\eta'} &= (\boldsymbol{\tau}_2, \mathbf{n}_x) \frac{\partial Q}{\partial \mathbf{n}_x} + (\boldsymbol{\tau}_2, \mathbf{n}_y) \frac{\partial Q}{\partial \mathbf{n}_y} + (\boldsymbol{\tau}_2, \mathbf{n}_z) \frac{\partial Q}{\partial \mathbf{n}_z}, \\ Q_{\zeta'} &= (\boldsymbol{\tau}_3, \mathbf{n}_x) \frac{\partial Q}{\partial \mathbf{n}_x} + (\boldsymbol{\tau}_3, \mathbf{n}_y) \frac{\partial Q}{\partial \mathbf{n}_y} + (\boldsymbol{\tau}_3, \mathbf{n}_z) \frac{\partial Q}{\partial \mathbf{n}_z}.\end{aligned}$$

More details about spatial reconstruction can be found in previous work [27, 37, 43].

## 2.4 Temporal Discretization

With the time dependent flux function, the two-stage fourth-order time-accurate method [36, 37] can be adopted for temporal discretization. Consider the time dependent numerical flux as Eq.(7), the state  $\widehat{Q}^{n+1}$  at  $t_{n+1} = t_n + \Delta t$  can be updated with

$$\begin{aligned}\widehat{Q}^* &= Q^n + \frac{1}{2} \Delta t \mathcal{L}(\widehat{Q}^n) + \frac{1}{8} \Delta t^2 \partial_t \mathcal{L}(\widehat{Q}^n), \\ \widehat{Q}^{n+1} &= \widehat{Q}^n + \Delta t \mathcal{L}(\widehat{Q}^n) + \frac{1}{6} \Delta t^2 (\partial_t \mathcal{L}(\widehat{Q}^n) + 2 \partial_t \mathcal{L}(\widehat{Q}^*)),\end{aligned}\tag{13}$$

where the subscripts are omitted. For hyperbolic equations, it can be proved that the above temporal discretization Eq.(13) provides a fourth-order time accurate solution for  $\widehat{Q}^{n+1}$ . To implement two-stage fourth-order method for Eq.(7), a linear function is used to approximate the time dependent numerical flux

$$\widehat{\mathbf{F}}_{i+1/2,j,k}(t) \approx \widehat{\mathbf{F}}_{i+1/2,j,k}^n + \partial_t \widehat{\mathbf{F}}_{i+1/2,j,k}^n(t - t_n).\tag{14}$$

Integrating Eq.(14) over  $[t_n, t_n + \Delta t/2]$  and  $[t_n, t_n + \Delta t]$ , the following two equations read

$$\widehat{\mathbf{F}}_{i+1/2,j,k}^n \Delta t + \frac{1}{2} \partial_t \widehat{\mathbf{F}}_{i+1/2,j,k}^n \Delta t^2 = \int_{t_n}^{t_n + \Delta t} \widehat{\mathbf{F}}_{i+1/2,j,k}(t) dt,$$

$$\frac{1}{2} \widehat{\mathbf{F}}_{i+1/2,j,k}^n \Delta t + \frac{1}{8} \partial_t \widehat{\mathbf{F}}_{i+1/2,j,k}^n \Delta t^2 = \int_{t_n}^{t_n + \Delta t/2} \widehat{\mathbf{F}}_{i+1/2,j,k}(t) dt.$$

The coefficients at the initial stage can be determined by solving the linear system, and the flow variables  $\widehat{\mathbf{Q}}^*$  at the intermediate stage can be updated. Similarly,  $\mathcal{L}(\widehat{\mathbf{Q}}^*)$  and  $\partial_t \mathcal{L}(\widehat{\mathbf{Q}}^*)$  at the intermediate state can be constructed and  $\widehat{\mathbf{Q}}^{n+1}$  can be updated as well. More details of the two-stage fourth-order temporal discretization can be found in refereed paper [36, 37]. Up to this point, the so-called HGKS in general curvilinear coordinate is presented with the second-order gas-kinetic solver, as well as the fifth-order spatial reconstruction and two-stage fourth-order time discretization. With the mesh given by the discretized grid points, both the order of accuracy and geometric conservation law can be well preserved by the current scheme.

### 3 Implicit Large Eddy Simulation with HGKS-cur

In this section, numerical tests from the nearly incompressible flow to the supersonic one will be presented to validate the HGKS-cur. For the numerical examples of this section, the grid points are given by analytical transformations or discretized points. While, the dimension-by-dimension Lagrangian interpolation is used for spatial accuracy in all the meshes. For following smooth flows without discontinuities, the collision time takes

$$\tau = \frac{\mu}{p},$$

where  $\mu$  is the dynamic viscous coefficient and  $p$  is the pressure at the cell interface. The ideal gas is assumed and the ratio of specific heat  $\gamma = 1.4$  is adopted. It is well known that the BGK scheme corresponds to unit Prandtl number. To achieve the targeted Prandtl number, the Prandtl number is modified by modifying energy flux as previous work [35].

Due to the explicit computation of HGKS, a parallel strategy has been developed, where the two-dimensional domain decomposition is used [28]. The procedure is the only data communication of the algorithm, which is handled by the MPI libraries. The total number of cells is  $N_x \times N_y \times N_z$ , and the computational domain is divided into  $n_y$  parts in  $y$ -direction,  $n_z$  parts in  $z$ -direction and no division is used in  $x$ -direction. The processor  $P_{jk}$ ,  $j = 0, \dots, n_y - 1, k = 0, \dots, n_z - 1$  handles a sub-domain with  $N_x \times n_{y_j} \times n_{z_k}$  cells. The scalability of our MPI code is examined by measuring the wall clock time against the number of processors, which scales properly with the number of processors used. It is indicated that the data communication crossing nodes costs a little time and the computation for flow field is the dominant one. Thus, the same parallel strategy is applied in current HGKS-cur for following numerical tests.

Large eddy simulation is proposed to solve the filtered Navier–Stokes equations with resolvable turbulent structures above the inertial scale. Explicit eddy-viscosity large eddy simulation has widely been used in unsteady incompressible and compressible separated turbulent flows. Different with the eLES, iLES takes the built-in numerical dissipation as the SGS dissipation. Due to the lower computational costs and better performance, iLES has gradually been utilized in LES community [46–50]. The quantitative analysis between iLES and eLES with HGKS [30] shows that iLES outperforms eLES on the exact same unresolved grids for the key statistical quantities. In this section, the performance of HGKS-cur is validated for the iLES of turbulent flows with curved boundary.

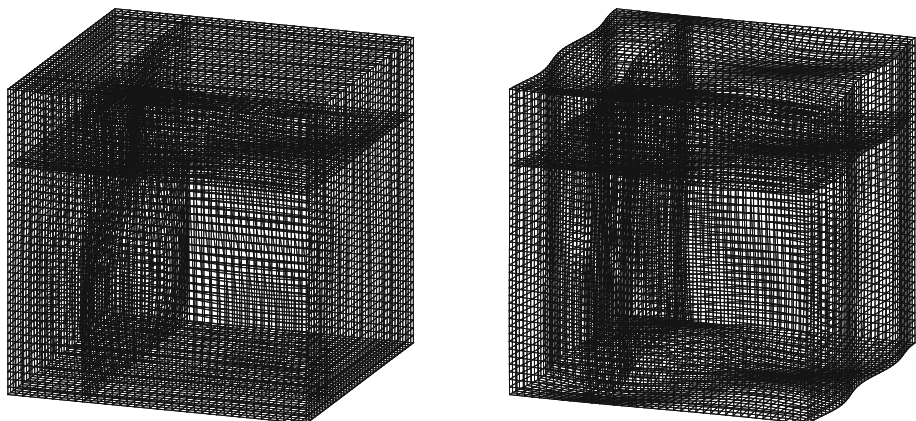


**Fig. 1** Accuracy test: the curvilinear physical meshes for mesh 1 (left) and mesh 2 (right) with  $40^3$  cells

### 3.1 Accuracy Tests

In this case, the advection of density perturbation is presented for accuracy tests and the validation of geometric conservation law [11, 51]. For the three-dimensional (3D) case, the initial condition is set as

$$\begin{aligned} \rho_0(x, y, z) &= 1 + 0.2 \sin(\pi(x + y + z)), \quad p_0(x, y, z) = 1, \\ U_0(x, y, z) &= 1, \quad V_0(x, y, z) = 1, \quad W_0(x, y, z) = 1. \end{aligned}$$

In the computation, the physical domain is  $[0, 2] \times [0, 2] \times [0, 2]$ . The periodic boundary conditions are applied at all boundaries, and the exact solutions are

$$\begin{aligned} \rho(x, y, z, t) &= 1 + 0.2 \sin(\pi(x + y + z - 3t)), \quad p(x, y, z, t) = 1, \\ U(x, y, z, t) &= 1, \quad V(x, y, z, t) = 1, \quad W(x, y, z, t) = 1. \end{aligned}$$

For the curvilinear mesh, two types of mesh are tested, which are given as follows

$$\begin{aligned} \text{mesh 1: } &\begin{cases} x = \xi + 0.05 \sin(\pi\xi) \sin(\pi\eta) \sin(\pi\zeta), \\ y = \eta + 0.05 \sin(\pi\xi) \sin(\pi\eta) \sin(\pi\zeta), \\ z = \zeta + 0.05 \sin(\pi\xi) \sin(\pi\eta) \sin(\pi\zeta), \end{cases} \\ \text{mesh 2: } &\begin{cases} x = \xi + 0.05 \sin(\pi\eta) \sin(\pi\zeta), \\ y = \eta + 0.05 \sin(\pi\zeta) \sin(\pi\xi), \\ z = \zeta + 0.05 \sin(\pi\xi) \sin(\pi\eta), \end{cases} \end{aligned}$$

where  $(\xi, \eta, \zeta) \in [0, 2] \times [0, 2] \times [0, 2]$  and the uniform cells are used in the computational domain, and the above meshes with  $40^3$  cells are shown in Fig. 1 as an example. The  $L^1$  and  $L^2$  errors and orders of accuracy at  $t = 2$  with  $N^3$  cells are given in Table 1 and Table 2. The expected accuracy can be achieved for the current HGKS-cur.

The GCL is also tested by the above meshes. The GCL is mainly about the maintenance of a uniform flow passing through a non-uniform non-orthogonal mesh. The initial condition for the three-dimensional case is

$$\rho_0(x, y, z) = 1, \quad p_0(x, y, z) = 1, \quad U_0(x, y, z) = 1, \quad V_0(x, y, z) = 1, \quad W_0(x, y, z) = 1.$$

**Table 1** Accuracy test: 3D advection of density perturbation for mesh 1

mesh 1	$L^1$ error	order	$L^2$ error	order
$10^3$	2.8315E-02		1.1198E-02	
$20^3$	1.3524E-03	4.3879	5.7195E-04	4.2912
$40^3$	5.7464E-05	4.5567	2.3528E-05	4.6034
$80^3$	2.7384E-06	4.3912	1.0882E-06	4.4344
$160^3$	1.5286E-07	4.1630	6.0120E-08	4.1779

**Table 2** Accuracy test: 3D advection of density perturbation for mesh 2

mesh 2	$L^1$ error	order	$L^2$ error	order
$10^3$	2.7971E-02		1.1473E-02	
$20^3$	1.1418E-03	4.6145	4.9546E-04	4.5334
$40^3$	4.5344E-05	4.6543	2.0510E-05	4.5943
$80^3$	2.5800E-06	4.1354	1.0528E-06	4.2839
$160^3$	1.5776E-07	4.0315	6.2671E-08	4.0703

**Table 3** Accuracy test: geometric conservation law for 3D meshes

mesh	mesh 1 $L^1$ error	$L^2$ error	mesh 2 $L^1$ error	$L^2$ error
$10^3$	6.2119E-15	2.7861E-15	5.8406E-15	2.6278E-15
$20^3$	8.2257E-15	3.6661E-15	7.4312E-15	3.3097E-15
$40^3$	1.2293E-14	5.4848E-15	1.1961E-14	5.3458E-15
$80^3$	2.1767E-14	9.7864E-15	2.1670E-14	9.7434E-15
$160^3$	4.6088E-14	2.0787E-14	4.5892E-14	2.0716E-14

The periodic boundary conditions are adopted as well. The  $L^1$  and  $L^2$  errors at  $t = 2$  are given in Table 3. The results show that the errors reduce to the machine zero, and the geometric conservation law is well preserved by the HGKS-cur.

### 3.2 Lid-Driven Cavity Flow

The lid-driven cavity problem is a benchmark for laminar flow simulations. The fluid is bounded by a unit cubic  $[0, 1] \times [0, 1] \times [0, 1]$  and driven by a uniform translation of the top boundary with  $Y = 1$ . Three-dimensional cavity-flow calculations have been carried out early [52]. In this case, the flow is simulated with Mach number  $Ma = 0.15$  and all the boundaries are isothermal and nonslip. To well resolve the boundary layer, the following local refined meshes are used

$$\begin{cases} x = \xi - 0.1 \sin(2\pi\xi), \\ y = \eta - 0.1 \sin(2\pi\eta), \\ z = \zeta - 0.1 \sin(2\pi\zeta). \end{cases}$$

**Fig. 2** Lid-driven cavity flow: the non-uniform physical mesh with  $33^3$  cells

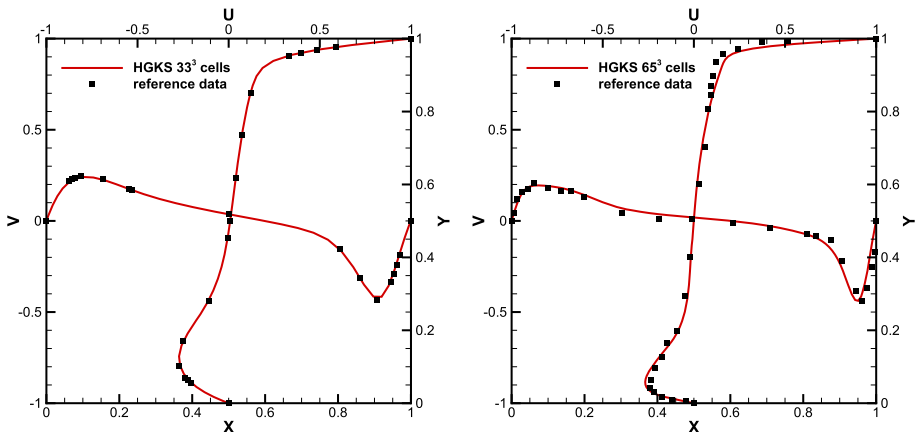
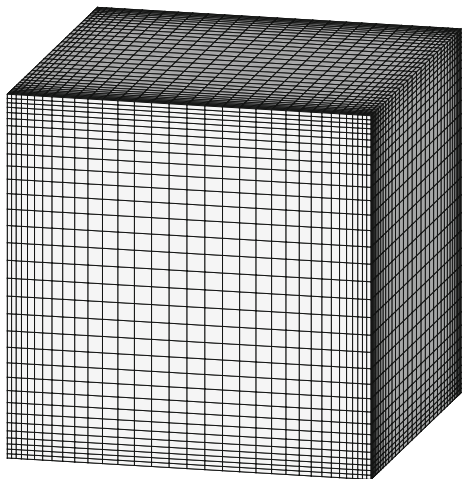


**Fig. 3** Lid-driven cavity flow:  $U$ -velocity profiles along the vertical centerline and  $V$ -velocity profiles along the horizontal centerline for  $Re = 1000$  (left) and  $3200$  (right)

Numerical simulations are conducted with Reynolds numbers  $Re = 1000$  and  $3200$ . For the case with  $Re = 1000$ , the convergent solution is obtained and the uniform mesh in the computational domain with  $33^3$  cells is used. The non-uniform physical meshes with  $33^3$  cells is shown in Figure 2. The flow at  $Re = 3200$  corresponds to unsteady solution, which have been studied extensively [53, 54]. The uniform mesh in the computational domain with  $65^3$  cells is used and the numerical results are averaged in 250 time period. The  $U$ -velocity profiles along the vertical centerline,  $V$ -velocity profiles along the horizontal centerline in the symmetry  $X - Y$  plane are shown in Figure 3. For these two cases, the results from the Chebyshev-collocation method [53] on a Gauss-Lobatto grid of size  $96^3$  for  $Re = 1000$  and the experimental data [54] for  $Re = 3200$  are adopted as the benchmark data, respectively. The agreement between them shows that current HGKS-cur is capable of simulating three-dimensional steady and unsteady laminar flows.

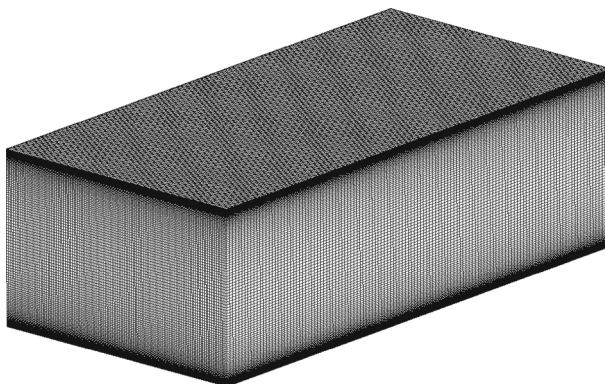


**Fig. 4** Compressible turbulent channel flow: the non-uniform physical mesh with  $128^3$  cells

### 3.3 Compressible Turbulent Channel Flow

Considering the simplicity of geometry and boundary conditions, the faithful computational studies of incompressible to hypersonic turbulent channel flow [1, 6, 14–16] have been carried out to study the mechanism of turbulent boundary layer. In this section, the compressible turbulent channel flow [14, 15] with bulk Mach number  $Ma = 1.5$  and bulk Reynolds number  $Re = 3000$  is tested with non-uniform mesh. In the computation, the physical domain is  $(x, y, z) \in [0, 4\pi H] \times [-H, H] \times [0, 4\pi H/3]$  and the computational domain takes  $(\xi, \eta, \zeta) \in [0, 4\pi H] \times [-1.5\pi H, 1.5\pi H] \times [0, 4\pi H/3]$ . In the computation, the coordinate transformation is given by

$$\begin{cases} x = \xi, \\ y = \tanh(b_g(\frac{\eta}{1.5\pi} - 1))/\tanh(b_g), \\ z = \zeta, \end{cases}$$

where  $b_g = 2$ . The mesh with  $128^3$  cells is given in Fig. 4 as an example. This case addresses the performance of HGKS-cur in non-uniform mesh for compressible wall-bounded turbulent flows. The periodic boundary conditions are used in streamwise  $x$ -direction and spanwise  $z$ -directions, and the non-slip and isothermal boundary conditions are used in wall-normal  $y$ -direction.

In current study, the fluid is initiated with density  $\rho = 1$  and the initial streamwise velocity  $U(y)$  profile is given by the perturbed Poiseuille flow profile

$$U(y) = 1.5(1 - y^2) + \text{white noise},$$

where the white noise is added with 10% amplitude of local streamwise velocity. The spanwise and wall-normal velocity is initiated with white noise. The initial non-dimensional parameters bulk Mach number  $Ma$  and bulk Reynolds number  $Re$  are defined as

$$Ma = \frac{U_b}{c_w}, \quad Re = \frac{\rho_b U_b H}{\mu_w},$$

where  $H = 1$  is the half height of the channel,  $c_w = \sqrt{\gamma RT_w}$  is the wall sound speed,  $\mu_w$  the wall molecular viscosity,  $T_w$  the wall temperature and  $R$  the gas constant. The viscosity  $\mu$  is determined by the power law as  $\mu(T) \propto T^{0.7}$ . The Prandtl number is defined as  $Pr = \mu c_p/\kappa$ ,

**Table 4** Compressible turbulent channel flow: Prandtl number and numerical parameters of the present and the reference simulations. “—” means that the data can not be find in the refereed paper

Case	Run	$Pr$	Physical domain	$N_x \times N_y \times N_z$	$\Delta Y_{min}^+ / Y_{N10}^+$	$\Delta X^+$	$\Delta Z^+$
Ref <sub>1</sub>	DNS	0.70	$4\pi H \times 2H \times 4\pi H/3$	$144 \times 90 \times 60$	0.10/8	19	12
Ref <sub>2</sub>	DNS	0.72	$4\pi H \times 2H \times 4\pi H/3$	$120 \times 180 \times 120$	0.36/-	23	7.60
Ref <sub>3</sub>	CLES	0.70	$4\pi H \times 2H \times 4\pi H/3$	$64 \times 65 \times 64$	0.50/-	43	14
$G_1$	iLES	0.70	$4\pi H \times 2H \times 4\pi H/3$	$128 \times 128 \times 128$	0.50/12.66	21.18	7.06
$G_2$	iLES	0.70	$2\pi H \times 2H \times 4\pi H/3$	$128 \times 128 \times 128$	0.50/12.66	10.59	7.06
$G_3$	iLES	1.0	$4\pi H \times 2H \times 4\pi H/3$	$128 \times 128 \times 128$	0.50/12.66	21.18	7.06
$G_4$	DNS	0.70	$4\pi H \times 2H \times 4\pi H/3$	$160 \times 160 \times 160$	0.40/9.50	16.92	5.64

where  $c_p$  is the specific heat at constant pressure and the  $\kappa$  is the heat conductivity. The bulk velocity  $U_b$  and bulk-averaged density  $\rho_b$  are defined as

$$U_b = \int_{-H}^H U(y) dy, \quad \rho_b = \int_{-H}^H \rho(y) dy.$$

The plus unit  $Y^+$  and plus velocity  $U^+$  are defined as

$$Y^+ = \frac{\rho u_\tau y}{\mu}, \quad U^+ = \frac{U}{u_\tau},$$

with the friction velocity  $u_\tau$  and the wall shear stress  $\tau_w$  as

$$u_\tau = \sqrt{\frac{\tau_w}{\rho_w}}, \quad \tau_w = \mu_w \frac{\partial U}{\partial y} \Big|_w.$$

The friction Mach number  $Ma_\tau$  and the friction Reynolds number  $Re_\tau$  are given by

$$Ma_\tau = \frac{u_\tau}{c_w}, \quad Re_\tau = \frac{H}{\delta_v}, \quad \delta_v = \frac{\mu_w}{\rho_w u_\tau}.$$

The heat flux  $q_w$  and the non-dimensional heat flux  $B_q$  of the wall are defined as

$$q_w = -\kappa \frac{\partial T}{\partial y} \Big|_w, \quad B_q = \frac{q_w}{\rho_w c_p u_\tau T_w}.$$

In this computation, the details of Prandtl number and numerical parameters are given in Table 4. The numerical results of DNS in refereed paper [14] and [15] are denoted as Ref<sub>1</sub> and Ref<sub>2</sub>, constrained large-eddy simulation (CLES) approach [55] is denoted as Ref<sub>3</sub>, and four cases  $G_1 - G_4$  are implemented by current HGKS-cur. CLES is implemented on the coarsest grid, which has succeeded in predicting compressible turbulent flows [56, 57]. The spectral method and B-spline collocation method is used by Ref<sub>1</sub> and Ref<sub>2</sub>, respectively. Compared with the set-up of case  $G_1$ , the half length of streamwise direction is used in case  $G_2$ . In addition, the unit Prandtl number  $Pr = 1$  is used for case  $G_3$ , and the finer mesh with  $160^3$  cells is applied in case  $G_4$ . Specifically,  $\Delta Y_{min}^+$  is the first grid space off the wall in the wall-normal direction, and  $Y_{N10}^+$  is the plus unit for the first ten points off the wall.  $\Delta X^+$  and  $\Delta Z^+$  are the equivalent plus unit for uniform streamwise and spanwise grids, respectively. For current HGKS-cur, cases  $G_1 - G_3$  are implemented as iLES, and case  $G_4$  is for DNS study.

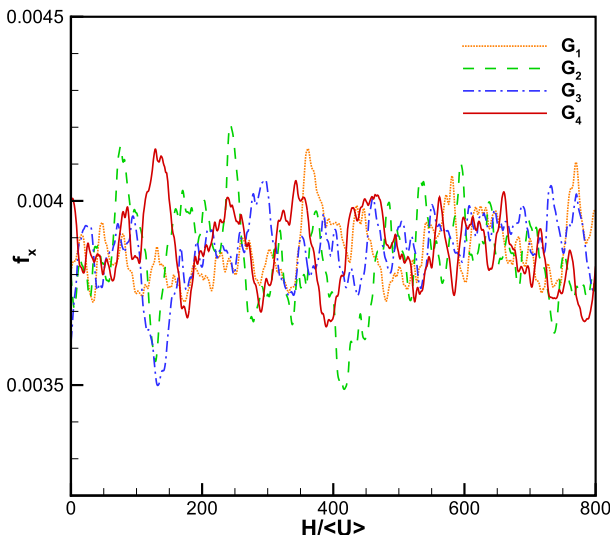


**Fig. 5** Compressible turbulent channel flow: the external force  $f_x$  for case  $G_1 - G_4$  after transition

**Table 5** Compressible turbulent channel flow: statistical quantities at the wall. “ – ” means that the data can not be find in the refereed paper

Case	Ref <sub>1</sub>	Ref <sub>2</sub>	Ref <sub>3</sub>	$G_1$	$G_2$	$G_3$	$G_4$
$\langle u_\tau \rangle$	0.054	–	0.054	0.053	0.053	0.051	0.053
$\langle Ma_\tau \rangle$	0.082	0.080	0.080	0.079	0.079	0.076	0.079
$\langle Re_\tau \rangle$	222	218	218	211	212	221	213
$\langle \rho_w \rangle$	1.355	–	1.354	1.355	1.363	1.476	1.356
$\langle q_w \rangle$	–0.0089	–	–	–0.0084	–0.0084	–0.0085	–0.0085
$\langle B_q \rangle$	–0.049	–0.048	–0.048	–0.047	–0.047	–0.045	–0.048

To excite channel flow to turbulence, a fixed external force  $f_x$  is exerted in the streamwise direction initially. After transition, the constant moment flux is used to determine the external force. More details of the implementation of external force can be found in Ref [28]. The external force after transition for cases  $G_1 - G_4$  are presented in Figure 5, which fluctuates to balance the wall shear stress. In the following analysis, 800 characteristic periodic time is used to obtain the statistically stationary turbulence. The averaging time is longer than that in the reference paper [14]. In what follows, note that the mean average over time and the  $X$ - and  $Z$ -directions is represented by  $\langle \cdot \rangle$ . Instantaneous slides of normalized streamwise velocity at  $Z = 0$  and  $Y^+ = 3.2$  for case  $G_1$  are shown in Figure 6, where the streamwise velocity is normalized by friction velocity  $u_\tau$ . The mean velocity is extracted for the slide at  $Y^+ = 3.2$ , and the high-speed streaks and low-speed streaks are clearly presented. The key statistical quantities at the wall are presented in Table 5. For current iLES with HGKS-cur, the cases  $G_1$  and  $G_4$  agree well with the refereed solutions, and  $G_1$  converges to  $G_4$ . Compared with the effect of large Prandtl number as case  $G_3$ , the smaller streamwise computational size as case  $G_2$  almost dose not affect the statistical variables at the wall. Table 5 shows that the large Prandtl number enlarges the mean friction Reynolds number  $Re_\tau$ , the density at the wall  $\rho_w$ ,

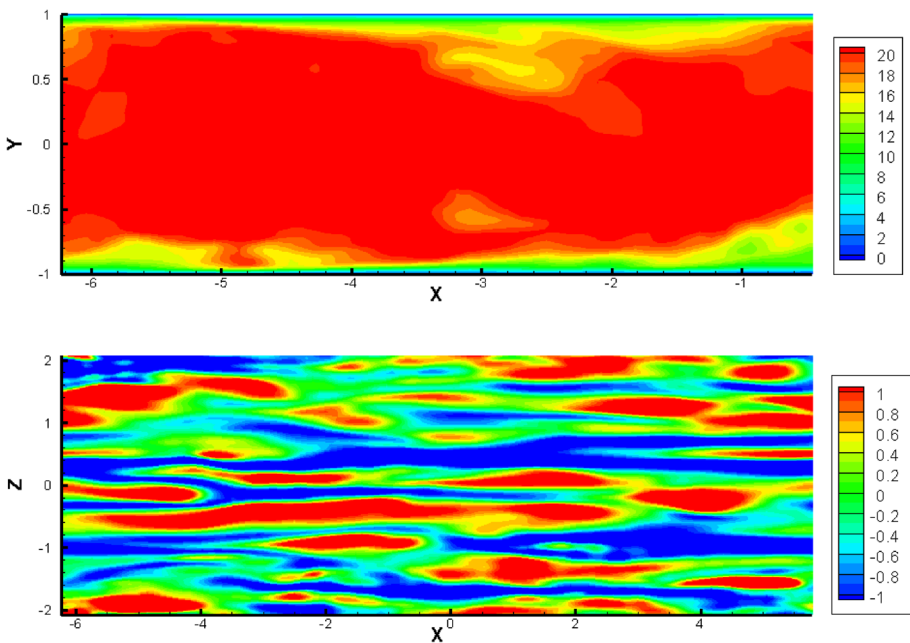


**Fig. 6** Compressible turbulent channel flow: instantaneous contour for case  $G_1$ , the streamwise velocity is normalized by friction velocity  $u_\tau$ . The upper is contour of instantaneous streamwise velocity at  $Z = 0$ , and the lower contour represents the instantaneous streamwise velocity at  $Y^+ = 3.2$  with extracting the mean velocity

and the friction non-dimensional heat flux  $B_q$ . It is known from dimensional analysis that the mean velocity and temperature profiles depend on the non-dimensional heat flux  $B_q$ , and the friction Mach number  $M_\tau$  [15]. As the ratio of specific heats  $\gamma$  and the specific heat at constant pressure  $c_p$  are constants, the mean velocity and temperature profiles depend on the Prandtl number, and this will be validated in the following part.

To further quantify the performance of HGKS-cur, the mean density  $\langle \rho \rangle$ , temperature  $\langle T \rangle$  and Mach number  $\langle Ma \rangle$ , the normalized root-mean-square of density  $\langle \rho_{rms} \rangle / \langle \rho \rangle$ , temperature  $\langle T'_{rms} \rangle / \langle T \rangle$ , and the turbulent Mach number  $M_t$  are presented in Fig. 7. The turbulent Mach number is defined as  $M_t = q / \langle c \rangle$ , where  $q^2 = \langle U'_i U'_i \rangle$ ,  $U'_i = U_i - \langle U_i \rangle$ , and  $c$  is the local sound speed. The root mean square is defined as  $\phi'_{rms} = \sqrt{(\phi - \langle \phi \rangle)^2}$ , where  $\phi$  represents the density, temperature and velocity. For current iLES with HGKS-cur, Fig. 7 shows that case  $G_1$  converges to case  $G_4$ , and both of them agree well with the refereed DNS solutions. The smaller streamwise computational domain as case  $G_2$  slightly changes the first-order statistical quantities but deviates the root-mean-square of density and temperature obviously. The numerical behavior of case  $G_2$  indicates the streamwise computational size should be adopted as previous study [14], where the one-dimensional Fourier spectral has been used to validate the physical domain is large enough to resolve the streamwise turbulent structures. In terms of the effect of Prandtl number, the large Prandtl number  $Pr = 1$  changes the mean density, temperature and Ma number profiles greatly. The large Prandtl number also enlarges the peak of root-mean square of density and temperate, while reduces the peak value of turbulent Mach number. For compressible turbulence simulation using HGKS-cur, it is

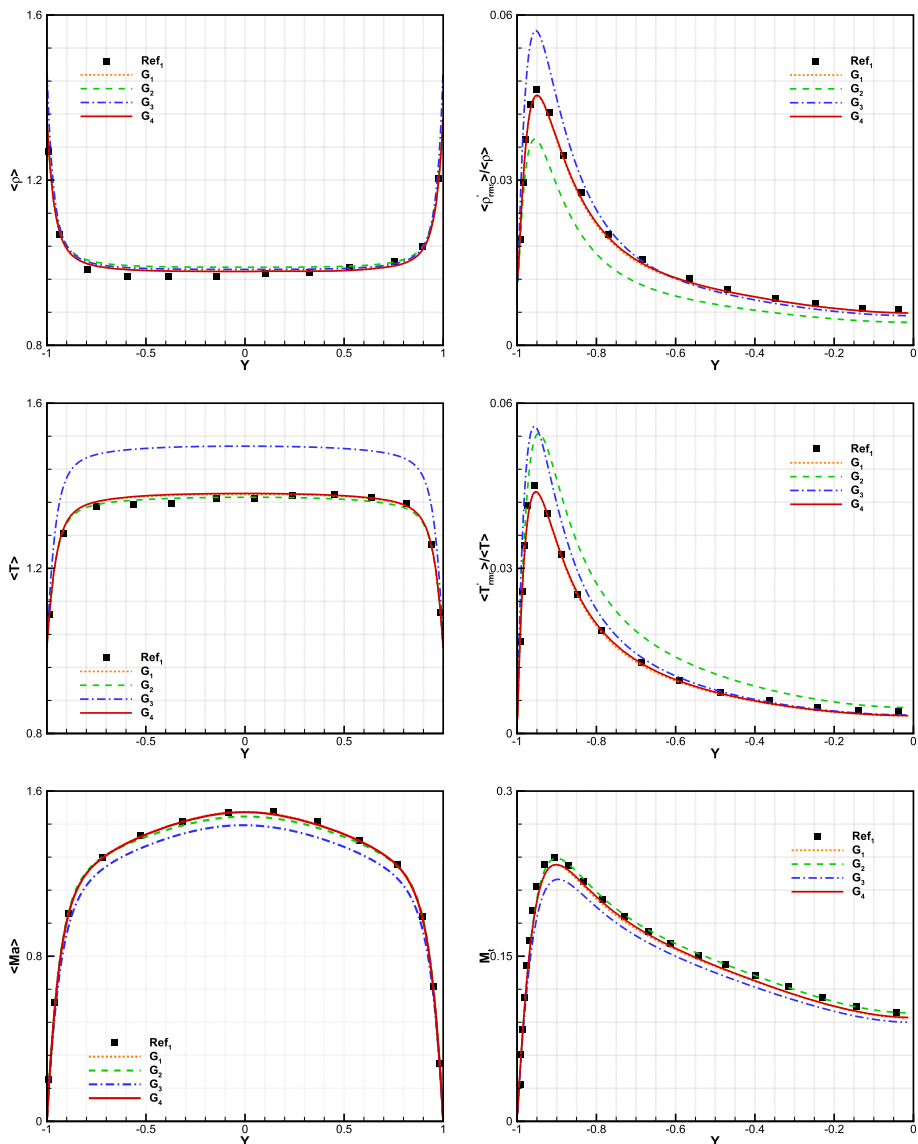


**Fig. 7** Compressible turbulent channel flow: the mean density  $\langle \rho \rangle$ , temperature  $\langle T \rangle$  and Mach number  $\langle Ma \rangle$  (left column), and the normalized root-mean-square of density  $\langle \rho'_{rms} \rangle / \langle \rho \rangle$ , temperature  $\langle T'_{rms} \rangle / \langle T \rangle$ , turbulent Mach number  $M_t$  (right column)

necessary to modify the Prandtl number to the targeted one [35]. Otherwise, the statistical thermodynamic and kinematic quantities will deviate from the expected values greatly. For current supersonic turbulent channel flow, the Mach number is  $Ma = 1.5$ , while the peak values of the turbulent Mach number  $M_t$  is less than 0.25. This means no strong shock-lets in such case, so spectral method [14] works well. The performance of case  $G_1$  and  $G_4$  confirms the high-accuracy flow-fields has been obtained by the HGKS-cur with non-uniform grids.

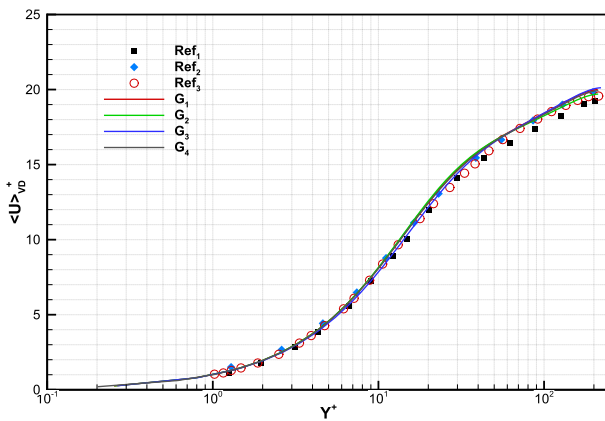


**Fig. 8** Compressible turbulent channel flow: VD transformation of streamwise velocity profiles  $\langle U \rangle_{VD}^+$

In order to account for the mean property of variations caused by compressibility, the Van Driest (VD) transformation [58] for the mean velocity, i.e., density-weighted velocity, is considered

$$\langle U \rangle_{VD}^+ = \int_0^{\langle U \rangle^+} \left( \frac{\langle \rho \rangle}{\langle \rho_w \rangle} \right)^{1/2} d\langle U \rangle^+,$$

where the transformed velocity is expected to satisfy the incompressible log law [14]. The streamwise velocity profiles  $\langle U \rangle_{VD}^+$  with VD transformation are given in Fig. 8. Overall, the iLES with HGKS-cur is in reasonable agreement with the reference DNS solutions, and CLES also performs very well on coarse grids. The profiles of normalized Reynolds stress  $-\langle \rho U' V' \rangle / \langle \tau_w \rangle$  and the turbulence intensities (the root-mean-square velocities as  $\langle U'_{rms} \rangle$ ,  $\langle V'_{rms} \rangle$ ,  $\langle W'_{rms} \rangle$ ) are presented in Fig. 9. Case  $G_1$  converges to the case  $G_4$ , and both of them agree well with the refereed solutions. The smaller streamwise computational domain as case  $G_2$  and the large Prandtl number case  $G_3$  deviate obviously from the refereed solutions. This confirms again that the enough streamwise computational size and targeted Prandtl number are essential in compressible wall-bounded turbulence simulations. The computational domain and the Prandtl number should be stressed for the iLES of compressible turbulent channel flow. The total Reynolds stress from CLES (containing the mean modeled SGS stress) coincides well with the DNS data. Even though CLES underestimates the values of turbulence intensities in the inner layer of flow, it still performs slightly better than the explicit LES with Smagorinsky model [55]. Based on the reasonable performance of case  $G_1$  and  $G_4$ , it can be concluded that iLES with current HGKS-cur on non-uniform grids offers the high-accuracy flow-fields for compressible turbulent channel flow.

### 3.4 Compressible Turbulent Flow Over Periodic Hills

The turbulent flow over periodically arranged hills in a channel [20–23] has been widely utilized to study the massive flow separation. In this section, the compressible turbulent flow over periodic hills with volumetric Mach number  $Ma_v = 0.2$  and cross-sectional Reynolds number  $Re_b = 2800$  is tested with curvilinear mesh. The geometry and a side view of the periodic hill are shown in Fig. 10. The physical domain is irregular with curved bottom wall

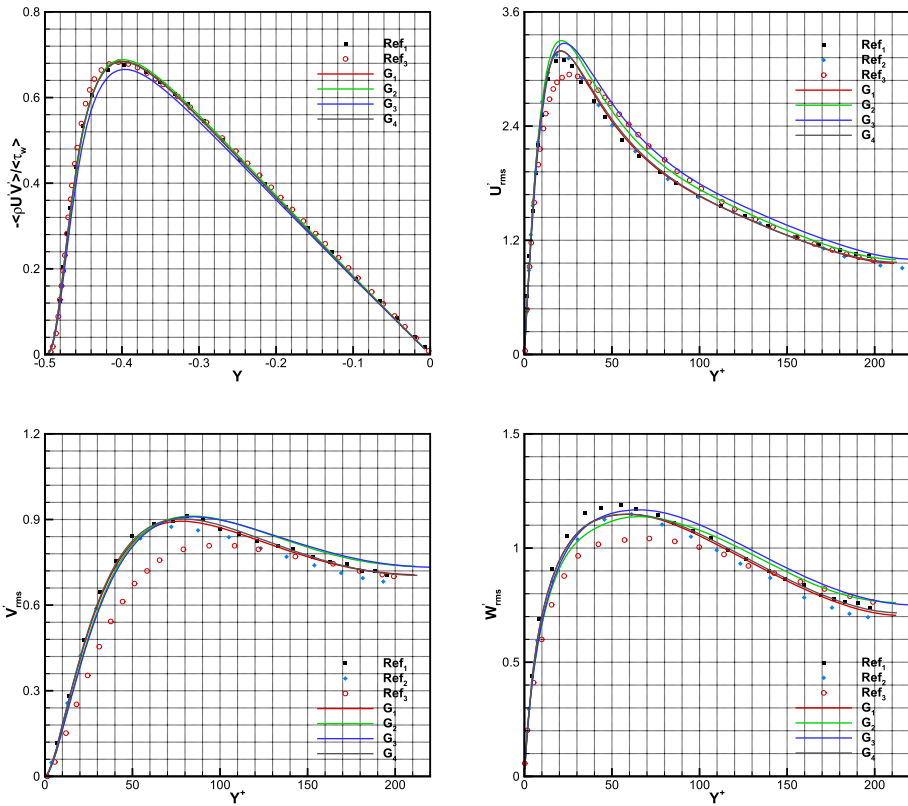


**Fig. 9** Compressible turbulent channel flow: profiles of normalized Reynolds stress  $-\langle \rho U' V' \rangle / \langle t_w \rangle$  and turbulence intensities  $\langle U'_{rms} \rangle$ ,  $\langle V'_{rms} \rangle$ ,  $\langle W'_{rms} \rangle$

and flat upper wall. The physical box extends over  $x \in [0, 9H]$  in the streamwise direction,  $y \in [0, 3.036H]$  in the wall-normal direction, and  $z \in [0, 4.5H]$  in the spanwise direction, respectively. The computational domain takes  $(\xi, \eta, \zeta) \in [0, 9H] \times [-1.5\pi H, 1.5\pi H] \times [0, 4.5H]$  as a regular cuboid. The hill height  $H = 1$  is chosen as the reference length for normalization. Equidistant grids are generated in spanwise and streamwise directions. The grid points on the bottom is taken from Ref [59], and the wall-normal grids is given by

$$y = \frac{3 - y_0}{2} \left( \tanh(b_g(\frac{\eta}{1.5\pi} - 1)) / \tanh(b_g) \right) + \frac{3 + y_0}{2},$$

where  $b_g = 1.7$ ,  $y_0$  is  $y$ -coordinate of bottom grid points and  $\eta$  distributes uniformly over  $[-1.5\pi, 1.5\pi]$ . The curvilinear mesh is given by the discretized grid points without analytical transformation. This case addresses the performance of HGKS-cur for the separated turbulence from the curved surface. The periodic boundary conditions are used in both streamwise  $x$ -direction and spanwise  $z$ -direction, and the non-slip and isothermal boundary conditions are used in upper wall and bottom wall.

In this study, the volumetric Mach number  $Ma_v$  is defined as

$$Ma_v = \frac{U_v}{c_w}, \quad U_v = \frac{1}{|\Omega|} \iiint_{\Omega} U d\Omega,$$

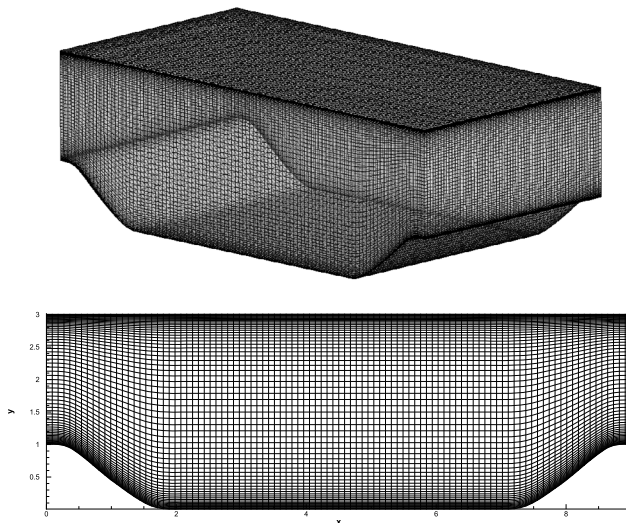


**Fig. 10** Compressible turbulent flow over periodic hills: the curvilinear 3D physical mesh with  $100^3$  cells (upper) and a side view of 2D mesh with  $100^2$  cells (bottom)

where  $|\Omega|$  is the volume of physical domain,  $c_w = \sqrt{\gamma RT_w}$  is the wall sound speed and  $T_w$  is the temperature at wall. The volumetric Reynolds number  $Re_v$  and the cross-sectional Reynolds number  $Re_b$  are defined as

$$Re_v = \frac{H}{\mu|\Omega|} \iiint_{\Omega} \rho U d\Omega, \quad Re_b = \frac{H}{\mu|S|} \iint_S (\rho U)|_{x=0} dS,$$

where  $|S|$  is the area of inlet cross section at the crest of hill. The cross-sectional Reynolds number  $Re_b$  can be determined by

$$Re_b = \frac{Re_v}{\Gamma}, \quad \Gamma = \frac{L_x L_y|_{x=0}}{\int_0^{L_x} L_y(x) dx} = 0.72,$$

where  $\Gamma$  is geometry factor,  $L_x = 9$  and  $L_y(x)$  the height of tunnel with respect to streamwise direction. The constant dynamic viscosity is used, and Prandtl number takes  $Pr = 0.72$ . In what follows, the mean average over the time and spanwise  $Z$ -direction is denoted by  $\langle \cdot \rangle$ . The mean friction coefficient  $C_f$  reads

$$C_f = \frac{\tau_w}{\langle \rho_b \rangle \langle U_b \rangle^2}, \quad \tau_w = \mu_w \frac{\partial \langle U \rangle}{\partial n}|_w,$$

where cross-sectional density  $\rho_b$  and cross-sectional velocity  $U_b$  are given by

$$\rho_b = \frac{1}{|S|} \iint_S \rho|_{x=0} dS, \quad U_b = \frac{1}{|S|} \iint_S U|_{x=0} dS.$$

The pressure coefficient  $C_p$  is defined as

$$C_p = \frac{\langle p \rangle - \langle p_x \rangle}{\langle \rho_b \rangle \langle U_b \rangle^2}, \quad p_x = \frac{1}{L_x} \int_0^{L_x} p(x) dx,$$

where  $p_x$  is the average pressure along the bottom wall. In this computation, cases  $H_1 - H_3$  are implemented by HGKS-cur as iLES. Details of volumetric Mach number  $Ma_v$ ,

**Table 6** Compressible turbulent flow over periodic hills: volumetric Mach number, numerical simulation parameters, and separation/reattachment locations of the present and reference simulations. "N/A" means no volumetric Mach number resulting from the incompressible simulation

Case	Run	$Ma_v$	$N_x \times N_y \times N_z$	$1 \times 10^6$ cells	$\Delta t/10^{-3}$	$X_{sep}$	$X_{reatt}$
Ref <sub>1</sub>	DNS	N/A	$464 \times 304 \times 338$	47.68	2.0	0.21	5.41
Ref <sub>2</sub>	LES	0.2	$128 \times 72 \times 69$	0.64	1.0	0.21	5.30
$H_1$	iLES	0.2	$100 \times 100 \times 100$	1.0	0.6	0.23	5.18
$H_2$	iLES	0.2	$200 \times 100 \times 100$	2.0	0.6	0.20	5.15
$H_3$	iLES	0.2	$400 \times 200 \times 200$	16.0	0.55	0.24	5.45

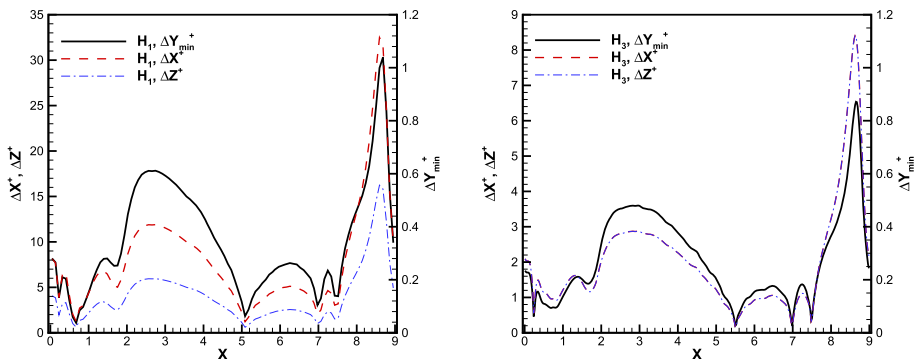


**Fig. 11** Compressible turbulent flow over periodic hills: grids spacing in the wall units for case  $H_1$  and  $H_3$ .  $\Delta Y_{min}^+$  is the first grid space off the bottom wall in the wall-normal direction

numerical parameters and separation/reattachment locations  $X_{sep}/X_{reatt}$  are presented in Table 6. DNS with immersed boundary technique on a non-equidistant staggered Cartesian mesh in conjunction with an incompressible second-order finite-volume solver [20] is referred as Ref<sub>1</sub>. Ref<sub>2</sub> is equipped with the fourth-order finite-volume scheme [21] for compressible LES. The approximate deconvolution model (ADM) is used for the compressible LES.  $\Delta t$  is the fixed time step used in simulations. Grids spacing in the wall units for case  $H_1$  and  $H_3$  are presented in Fig. 11, where  $\Delta Y_{min}^+$  is the first grid space off the bottom wall in the wall-normal direction. The unit plus is computed based on the post-processed mean flow fields, where each wall point has a local friction velocity. For current iLES study, the grids spacing in the wall units of case  $H_1$  is comparable with that in previous iLES [23]. While, the girds of case  $H_3$  is much finer, to implement the grid convergence study of iLES.

To keep the constant streamwise moment flux, the force is implemented as a spatially constant but temporally varying volume force in the streamwise direction [28]. The external force  $f_x$  and the cross-sectional Reynolds number  $Re_b$  after transition for cases  $H_1 - H_3$  are presented in Figure 12. Due to the variations of mass flux over cross section,  $Re_b$  is a function of time and fluctuates around 2730, which is slightly smaller than the targeted values 2800. These highly unsteady flow properties, lead to long sampling times to obtain sufficiently converged statistics. 400 characteristic periodic time is used for obtaining the statistically stationary turbulence for cases  $H_1$  and  $H_2$ . For case  $H_3$  with finest grids, more than 250 characteristic periodic time is adopted for a converged statistical study. The averaging time is comparable to that in the refereed paper [21]. The contour of mean streamwise velocity

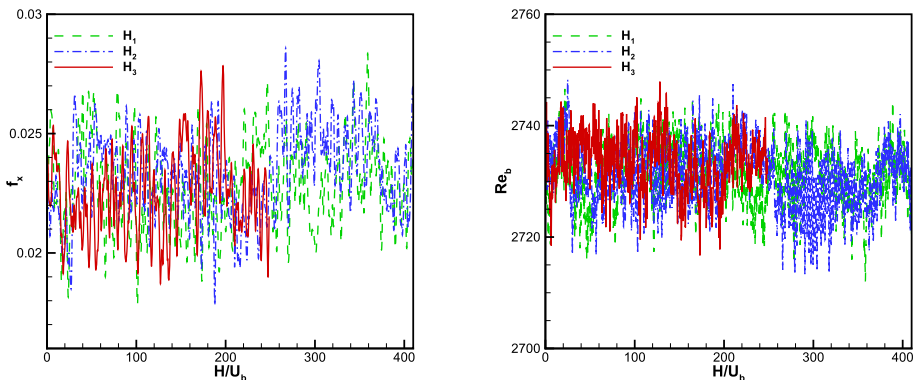


**Fig. 12** Compressible turbulent flow over periodic hills: external force  $f_x$  and cross-sectional Reynolds number  $Re_b$  for cases  $H_1 - H_3$

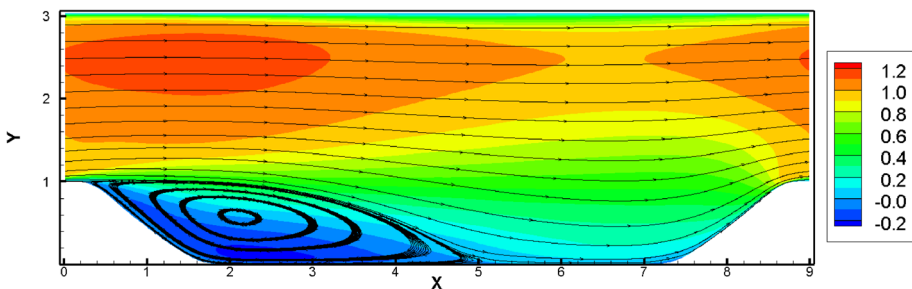


**Fig. 13** Compressible turbulent flow over periodic hills: contour of mean streamwise velocity and streamlines

and streamlines for case  $H_3$  is presented as Fig. 13. The instantaneous flow shows a periodic shedding of smaller vortices that are convected downstream, and the resulting separation bubble can be recognized clearly in the mean flow field. The friction coefficients and pressure coefficients along the bottom wall are presented in Fig. 14. The friction coefficients  $C_f$  of the current iLES and the explicit LES with ADM deviates slightly from the refereed DNS solution. The separation and reattachment locations shown in Table 6 are obtained based on these profiles of friction coefficient. The locations from current iLES are close to the refereed explicit LES and DNS solutions. For pressure coefficient  $C_p$ , current iLES agrees well with the refereed DNS solution, better than the explicit LES. Considering the less grids are used than DNS, the iLES of current HGKS-cur performs reasonably and provides efficient tool for compressible separated flow simulations.

Profiles at  $X = 1$ ,  $X = 2$ ,  $X = 4$  and  $X = 8$  of normalized mean velocities  $\langle U \rangle / \langle U_b \rangle$ ,  $\langle V \rangle / \langle U_b \rangle$  and normalized Reynolds stresses  $\langle U'U' \rangle / \langle U_b \rangle^2$ ,  $\langle V'V' \rangle / \langle U_b \rangle^2$  are presented in Fig. 15 and Fig. 16, respectively. For explicit LES with ADM, the density-weighted velocity and Reynolds stress are presented, while density-weighted procedure is not adopted in DNS and current iLES. The normalized mean streamwise velocity profiles  $\langle U \rangle / \langle U_b \rangle$  of HGKS-cur are in good agreement with the DNS solutions. The normalized mean wall-normal velocity profiles  $\langle V \rangle / \langle U_b \rangle$  of HGKS-cur are comparable with the results from the explicit LES. For second-order statistical Reynolds stresses, the iLES of HGKS-cur is comparable with the explicit LES. However, the explicit LES overpredicts the normalized Reynolds stresses,

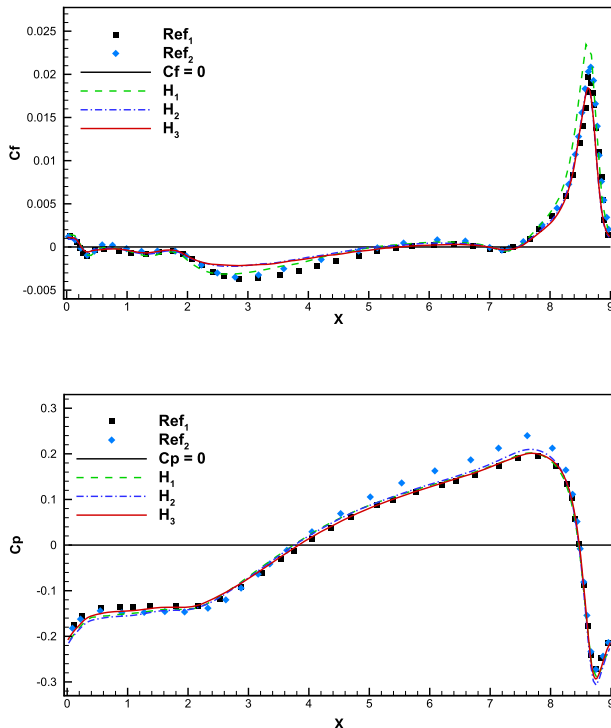


**Fig. 14** Compressible turbulent flow over periodic hills: frictional coefficients  $C_f$  and pressure coefficients  $C_p$  along the bottom wall

especially for  $\langle U' V' \rangle / \langle U_b \rangle^2$ . For this separated turbulent flow, it can be concluded that the explicit LES provides much stronger turbulent fluctuation information than the DNS. Thus, the explicit LES model may pollute current low-Reynolds number separated turbulent flow. While, the solutions from current iLES agree well with the DNS results, and the over-predicted behaviour seldom appears. For Reynolds stresses, case  $H_3$  with the finest grids indeed performs better than cases  $H_1$  and  $H_2$ . However, considering the computational costs of case  $H_3$ , the improvement is not so worthwhile. It is implied that coarse grids is enough for iLES when simulating low-Reynolds number separated turbulent flows. Overall, current iLES with HGKS-cur is comparable with the explicit LES with ADM using fourth-order finite-volume method [21].

HGKS-cur definitely provides a confident numerical tool for compressible separated flow simulations with curved boundary.

## 4 Conclusion

Within the two-stage fourth-order framework, HGKS in the general curvilinear coordinate (HGKS-cur) is developed for the first time to simulate the compressible wall-bounded turbulent flows.

Based on the coordinate transformation, the BGK equation is transformed from physical space to computational space. To deal with the meshes given by discretized points, the

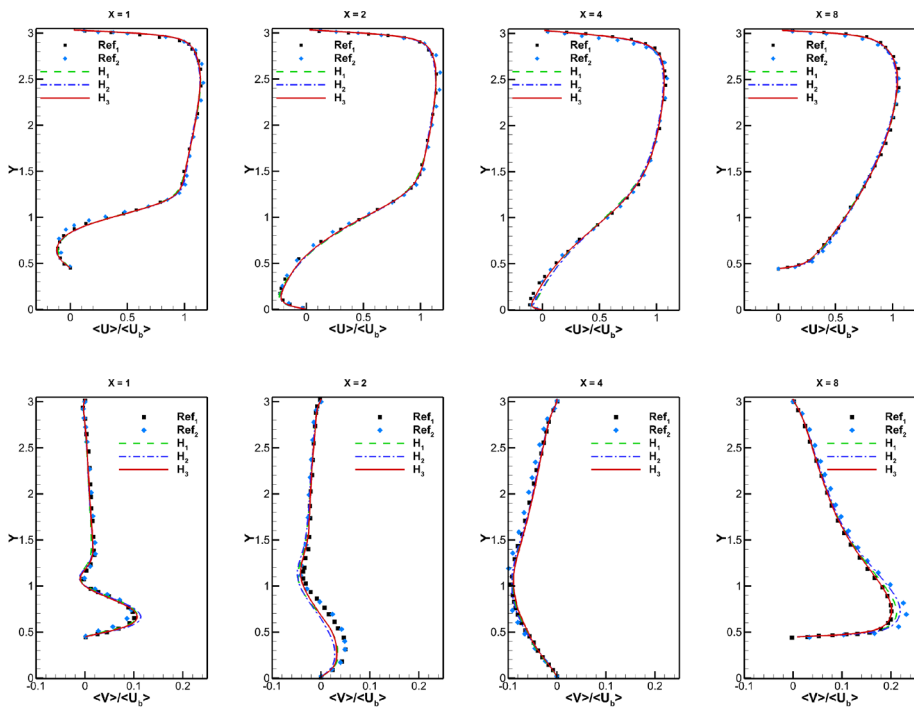


**Fig. 15** Compressible turbulent flow over periodic hills: profiles of normalized mean streamwise velocity  $\langle U \rangle / \langle U_b \rangle$  and normalized mean wall-normal velocity  $\langle V \rangle / \langle U_b \rangle$

geometrical metrics need to be reconstructed at quadrature points of control volumes and cell interfaces by the dimension-by-dimension Lagrangian interpolation and the geometrical conservation law can be preserved. To achieve high-order accuracy, WENO reconstruction is implemented to reconstruct the cell averaged Jacobian and the Jacobian-weighted conservative variables. The two-stage fourth-order method, which was developed for spatial-temporal coupled flow solvers, is used for temporal discretization. The numerical tests for inviscid and laminar flows validate the accuracy and geometrical conservation law of HGKS-cur. As a direct application, current scheme is implemented for iLES in compressible wall-bounded turbulence, including the compressible turbulent channel flow and compressible turbulent flow over periodic hills. The simulation results are in good agreement with the refereed spectral method and the high-order finite-volume method.

Current work confirms the capability of HGKS-cur as a powerful tool for the iLES in compressible wall-bounded turbulent flows and massively separated flows with curved boundary.

More challenging examples using HGKS-cur at higher Mach numbers and different flow configurations will be investigated in the future.

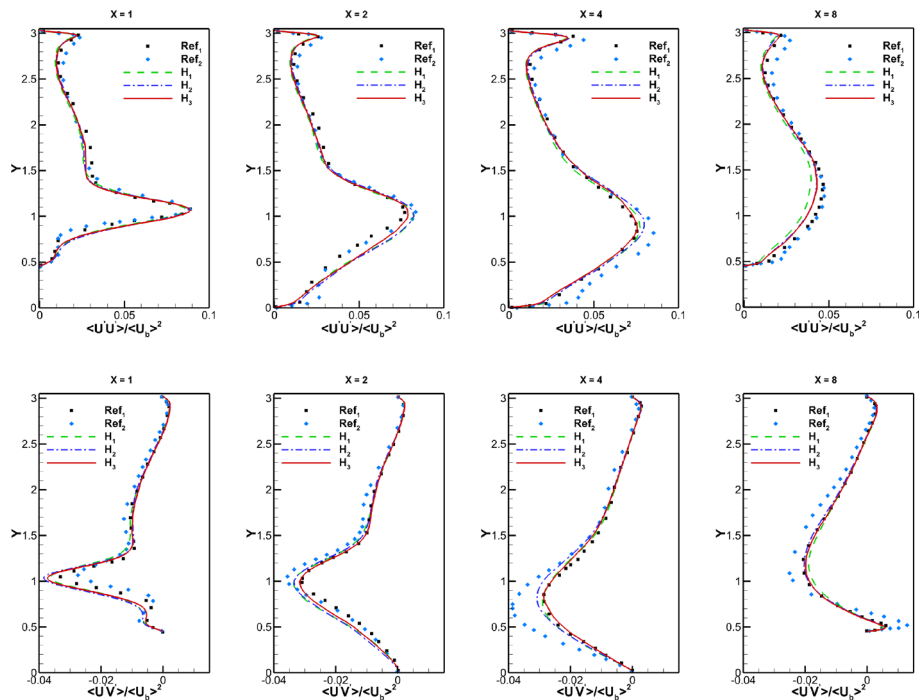


**Fig. 16** Compressible turbulent flow over periodic hills: profiles of normalized Reynolds stresses  $\langle U'U' \rangle / \langle U_b \rangle^2$  and  $\langle U'V' \rangle / \langle U_b \rangle^2$

**Acknowledgements** The authors would like to thank TaiYi supercomputers in the SUSTech for providing high performance computational resources.

**Funding** This research is supported by Beijing Natural Science Foundation (1232012), National Natural Science Foundation of China (12471364, 11701038, 12172316), and National Key R & D Program of China (2022YFA1004500).

**Data Availability** Data will be made available on request.

## Declarations

**Conflict of interest** The authors declare that they have no known competing financial interests or personal relationships that could have appeared to influence the work reported in this paper.

## References

1. Kim, J., Moin, P., Moser, R.: Turbulence statistics in fully developed channel flow at low Reynolds number. *J. Fluid. Mech.* **177**, 133–166 (1987)
2. Moin, P., Mahesh, K.: Direct numerical simulation: a tool in turbulence research. *Annu. Rev. Fluid Mech.* **30**, 539–578 (1998)
3. Manabe, S., Smagorinsky, J., Strickler, R.F.: Simulated climatology of a general circulation model with a hydrologic cycle. *Mon. Wea. Rev.* **93**, 769–798 (1965)
4. Sagaut, P.: Large eddy simulation for incompressible flows: an introduction. Springer Science & Business Media (2006)

5. Wang, L.P., Chen, S.Y., Brasseur, J.G., Wyngaard, J.C.: Examination of hypotheses in the Kolmogorov refined turbulence theory through high-resolution simulations. part 1. velocity field. *J. Fluid Mech.* **309**, 113–156 (1996)
6. Lee, M., Moser, R.: Direct numerical simulation of turbulent channel flow up to  $Re_\tau \approx 5200$ . *J. Fluid. Mech.* **774**, 395–415 (2015)
7. Chen, S.Y., Doolen, G.D.: Lattice boltzmann method for fluid flows. *Annu. Rev. Fluid Mech.* **30**, 329–364 (1998)
8. Yu, H.D., Girimaji, S.S., Luo, L.S.: Lattice boltzmann simulations of decaying homogeneous isotropic turbulence. *Phys. Rev. E* **71**, 016708 (2005)
9. Lele, S.K.: Compact finite difference schemes with spectral-like resolution. *J. Comput. Phys.* **103**, 16–42 (1992)
10. Fu, D.X., Ma, Y.W.: A high order accurate difference scheme for complex flow fields. *J. Comput. Phys.* **134**, 1–15 (1997)
11. Deng, X.G., Mao, M.L., Tu, G.H., Liu, H.Y., Zhang, H.X.: Geometric conservation law and application to high-order finite difference schemes with stationary grids. *J. Comput. Phys.* **230**, 1100–1115 (2011)
12. Samtaney, R., Pullin, D.I., Kosović, B.: Direct numerical simulation of decaying compressible turbulence and shocklet statistics. *Phys. Fluids* **13**, 1415–1430 (2001)
13. Wang, J.C., Wang, L.P., Xiao, Z.L., Shi, Y., Chen, S.Y.: A hybrid numerical simulation of isotropic compressible turbulence. *J. Comput. Phys.* **229**, 5257–5279 (2010)
14. Coleman, G., Kim, J., Moser, R.: A numerical study of turbulent supersonic isothermal-wall channel flow. *J. Fluid. Mech.* **305**, 159–184 (1995)
15. Morinishi, Y., Tamano, S., Nakabayashi, K.: Direct numerical simulation of compressible turbulent channel flow between adiabatic and isothermal walls. *J. Fluid. Mech.* **502**, 273–308 (2004)
16. Ming, Y., Xu, C.X., Pirozzoli, S.: Genuine compressibility effects in wall-bounded turbulence. *Phys. Rev. Fluids* **4**, 123402 (2019)
17. Pirozzoli, S., Grasso, F., Gatski, T.B.: Direct numerical simulation and analysis of a spatially evolving supersonic turbulent boundary layer at  $M = 2.25$ . *Phys. Fluids* **16**, 530–545 (2004)
18. Liang, X., Li, X.L., Fu, D.X., Ma, Y.W.: DNS and analysis of a spatially evolving hypersonic turbulent boundary layer over a flat plate at Mach 8. *Sci. China Phys. Mech. Astron.* **42**, 282–293 (2012)
19. Franko, Kenneth J., Lele, Sanjiva K.: Breakdown mechanisms and heat transfer overshoot in hypersonic zero pressure gradient boundary layers. *J. Fluid. Mech.* **730**, 491–532 (2013)
20. Peller, N., Manhart, M.: (2004) DNS einer Kanalströmung mit periodisch angeordneten Hugeln, STAB Jahresbericht 16–18
21. Ziefler, J., Stoltz, S., Kleiser, L.: Large-eddy simulation of separated flow in a channel with streamwise periodic constrictions. *AIAA journal* **46**, 1705–1718 (2008)
22. Breuer, M., Peller, N., Rapp, C., Manhart, M.: Flow over periodic hills—Numerical and experimental study in a wide range of Reynolds numbers. *Computers & Fluids* **38**(2), 433–457 (2009)
23. Ponnampalam, B., Park, G.: DNS/LES simulations of separated flows at high Reynolds numbers, 45th AIAA Fluid Dynamics Conference (2015)
24. Adams, N.A.: Direct simulation of the turbulent boundary layer along a compression ramp at  $M = 3$  and  $Re_\theta = 1685$ . *J. Fluid. Mech.* **420**, 47–83 (2000)
25. Wu, M.W., Martin, M.: Direct numerical simulation of supersonic turbulent boundary layer over a compression ramp. *AIAA journal* **45**, 879–889 (2007)
26. Chen, L., Xiao, Z.L., Shi, Y.P., Chen, S.Y.: Constrained large-eddy simulation of supersonic turbulent boundary layer over a compression ramp. *J. Turbul.* **18**, 781–808 (2017)
27. Cao, G.Y., Pan, L., Xu, K.: Three dimensional high-order gas-kinetic scheme for supersonic isotropic turbulence I: criterion for direct numerical simulation. *Computers & Fluids* **192**, 104273 (2019)
28. Cao, G.Y., Pan, L., Xu, K.: High-order gas-kinetic scheme with parallel computation for direct numerical simulation of turbulent flows. *J. Comput. Phys.* **448**, 110739 (2022)
29. Cao, G.Y., Pan, L., Xu, K.: Three dimensional high-order gas-kinetic scheme for supersonic isotropic turbulence II: coarse-graining analysis of compressible  $K_{sgs}$  budget. *J. Comput. Phys.* **439**, 110402 (2021)
30. Cao, G.Y., Zhao, W.J., Chen, S.Y.: Quantitative analysis on implicit large eddy simulation. *Phys. Fluids* **34**, 105103 (2022)
31. Zhao, W.J., Cao, G.Y., Wang, J.C., Xu, K.: High-order gas-kinetic schemes with non-compact and compact reconstruction for implicit large eddy simulation. *Computers and Fluids* **256**, 105846 (2023)
32. Bhatnagar, P.L., Gross, E.P., Krook, M.: A Model for Collision Processes in Gases I: Small Amplitude Processes in Charged and Neutral One-Component Systems. *Phys. Rev.* **94**, 511–525 (1954)
33. Chapman, S., Cowling, T.G.: The Mathematical theory of Non-Uniform Gases, 3rd edn. Cambridge University Press (1990)

34. Xu, K.: Gas kinetic schemes for unsteady compressible flow simulations, Lecure Note Ser. 1998-03, Von Karman Institute for Fluid Dynamics Lecture (1998)
35. Xu, K.: A gas-kinetic BGK scheme for the Navier-Stokes equations and its connection with artificial dissipation and Godunov method. *J. Comput. Phys.* **171**, 289–335 (2001)
36. Li, J.Q., Du, Z.F.: A two-stage fourth order time-accurate discretization for Lax-Wendroff type flow solvers I. hyperbolic conservation laws. *SIAM J. Sci. Computing* **38**, 3046–3069 (2016)
37. Pan, L., Xu, K., Li, Q.B., Li, J.Q.: An efficient and accurate two-stage fourth-order gas-kinetic scheme for the Navier-Stokes equations. *J. Comput. Phys.* **326**, 197–221 (2016)
38. Ji, X., Zhao, F., Shyy, W., Xu, K.: A family of high-order gas-kinetic schemes and its comparison with riemann solver based high-order methods. *J. Comput. Phys.* **356**, 150–173 (2018)
39. Zhao, F., Ji, X., Shyy, W., Xu, K.: Compact higher-order gas-kinetic schemes with spectral-like resolution for compressible flow simulations. *Adv. Aerodyn.* **1**, 13 (2019)
40. Righi, M.: A gas-kinetic scheme for turbulent flow. *Turbul Combust* **97**, 121–139 (2016)
41. Tan, S., Li, Q.B., Xiao, Z.X., Fu, S.: Gas kinetic scheme for turbulence simulation. *Aerospace Sci. Technol.* **78**, 214–27 (2018)
42. Cao, G.Y., Su, H.M., Xu, J.X., Xu, K.: Implicit high-order gas kinetic scheme for turbulence simulation. *Aerospace Science and Technology* **92**, 958–971 (2019)
43. Pan, L., Xu, K.: High-order gas-kinetic scheme in curvilinear coordinates for the Euler and Navier-Stokes solutions, *Commun. Comput. Phys.* **28**, 1321–1351 (2020)
44. Liu, X.D., Osher, S., Chan, T.: Weighted essentially non-oscillatory schemes. *J. Comput. Phys.* **115**, 200–212 (1994)
45. Jiang, G.S., Shu, C.W.: Efficient implementation of weighted ENO schemes. *J. Comput. Phys.* **126**, 202–228 (1996)
46. Boris, J., Grinstein, F.F., Oran, E., Kolbe, R.: New insights into large eddy simulation. *Fluid Dyn Res* **10**, 199–228 (1992)
47. Grinstein, F.F., Margolin, L.G., William, J.R.: Implicit large eddy simulation, vol. 10. Cambridge University Press, Cambridge (2007)
48. Hu, X.Y., Nikolaus, A.A.: Scale separation for implicit large eddy simulation. *J. Comput. Phys.* **230**, 7240–7249 (2011)
49. Lombard, J., Moxey, D., Sherwin, S., Hoessler, J., Dhandapani, S., Taylor, M.: Implicit large-eddy simulation of a wingtip vortex. *AIAA Journal* **54**, 506–518 (2016)
50. Moser, R., Haering, S., Yalla, G.: Statistical properties of subgrid-scale turbulence models. *Annu. Rev. Fluid Mech.* **53** (2021)
51. Xu, D., Deng, X.G., Chen, Y.M., Dong, Y.D., Wang, G.X.: On the free stream preservation of finite volume method in curvilinear coordinates. *Computers & Fluids* **129**, 20–32 (2016)
52. Goda, K.: A multistep technique with implicit difference schemes for calculating two- or three-dimensional cavity flows. *J. Comput. Phys.* **30**, 76–95 (1979)
53. Albensoeder, S., Kuhlmann, H.C.: Accurate three-dimensional lid-driven cavity flow. *J. Comput. Phys.* **206**, 536–558 (2005)
54. Prasad, A.K., Koseff, J.R.: Reynolds-number and end-wall effects on a lid-driven cavity flows. *Phys. Fluids A* **1**, 208–225 (1989)
55. Jiang, Z., Xiao, Z.L., Shi, Y.P., Chen, S.Y.: Constrained large-eddy simulation of wall-bounded compressible turbulent flows. *Phys. Fluids* **25**, 106102 (2013)
56. Hong, K.R., Xia, Z.H., Shi, Y.P., Xiao, Z.L., Chen, S.Y.: Constrained large-eddy simulation of compressible flow past a circular cylinder, *Commun. Comput. Phys.* **15**, 388–421 (2014)
57. Chen, L., Xiao, Z.L., Shi, Y.P., Chen, S.Y.: Constrained large-eddy simulation of supersonic turbulent boundary layer over a compression ramp. *Journal of Turbulence* **18**, 781–808 (2017)
58. Huang, P.G., Gary, N.C.: Van Driest transformation and compressible wall-bounded flows. *AIAA journal* **32**, 2110–2113 (1994)
59. Gloerfelt, X., Cinnella, P.: Benchmark database: 2D periodic hill flow, <https://www.researchgate.net/publication/315413324-Benchmark-database-2D-periodic-hill-flow>

**Publisher's Note** Springer Nature remains neutral with regard to jurisdictional claims in published maps and institutional affiliations.

Springer Nature or its licensor (e.g. a society or other partner) holds exclusive rights to this article under a publishing agreement with the author(s) or other rightsholder(s); author self-archiving of the accepted manuscript version of this article is solely governed by the terms of such publishing agreement and applicable law.